Article:

Lu, Y., Marsham, J.H. orcid.org/0000-0003-3219-8472, Tang, J. et al. (2 more authors) (2025) Summer Mesoscale Convective Systems in Convection-Permitting Simulation Using WRF Over East China. Journal of Geophysical Research: Atmospheres, 130 (8). e2025JD043653. ISSN 2169-897X

https://doi.org/10.1029/2025jd043653

Summer mesoscale convective systems in convection-permitting simulation using WRF over East China

Yutong Lu[1,2,3], J.H. Marsham[2], Jianping Tang[1,3]*, D.J. Parker[2,4,5], Juan Fang[1,3]

[1]School of Atmospheric Sciences, Nanjing University, Nanjing, China.

[2]Institute of Climate and Atmospheric Science (ICAS), School of Earth and Environment, University of Leeds, Leeds, United Kingdom.

[3]Key Laboratory of Mesoscale Severe Weather/Ministry of Education, Nanjing University, Nanjing, China.

[4]National Centre for Atmospheric Science, University of Leeds, Leeds, United Kingdom.

[5]NORCE Norwegian Research Centre AS, Bjerknes Center for Climate Research, Bergen, Norway.

Corresponding author: Jianping Tang (jptang@nju.edu.cn)

Key Points:

- 22-year regional WRF convection-permitting simulation reproduces MCS climatology in East China but overestimates intensive precipitation.
- WRF convection-permitting model captures the MCS diurnal cycle though produces an earlier peak adjacent to complex terrain.
- Shear effects on MCSs in East China could be captured by WRF convection-permitting model.

Abstract

Mesoscale convective systems (MCSs) are active precipitation systems in East China. The increasing frequency and intensity of MCSs highlight the need for better simulation and forecasting. This study conducted a 22-year (2000–2021) JJA simulation at a CP resolution (4 km grid spacing) using the WRF model (WRF-CPM) over East China. The WRF-CPM model's ability to reproduce MCSs was evaluated against satellite infrared-retrieved cloud top temperature, IMERG V06 precipitation, and global reanalysis data ERA5. Results show that WRF-CPM captures the observed MCS frequency and precipitation patterns but overestimates them in most areas, which might be related to the overestimated moisture and CAPE. The model also reproduces the eastward propagation of MCSs, albeit at a slightly faster speed and longer duration. MCSs in WRF-CPM exhibits realistic life cycles in terms of cloud top temperature, convective core area, and precipitation. WRF-CPM tends to overestimate rainfall frequency over 20 mm/h while underestimates rainfall per MCS, possibly due to an overestimated number and area. The model captures the diurnal cycle of MCSs well in most of East China, though it shows a 2-hour delay in southeast China and produces the peak a few hours earlier to the east of Tibetan Plateau. Total column water vapor (TCWV) and wind shear are well-established factors controlling MCS behavior and rainfall, yet capturing the effects remains a challenge for CP models. This study is the first to show that WRF-CPM can capture the shear effect on MCS precipitation, showing an increase in precipitation with stronger shear and higher TCWV.

Plain Language Summary

Mesoscale convective systems (MCSs) cause significant rainfall and extreme weather in East China during the summer. As these systems become more frequent and intense, better simulation and forecasting are needed. Traditional models struggle to accurately represent MCSs due to their coarse resolutions. This study used a high-resolution model (WRF-CPM) to simulate MCSs over East China from 2000–2021. The evaluation with satellite data showed that while WRF-CPM can accurately capture the spatial distribution of MCSs, it tends to generate too many MCSs. The eastward movement of MCSs is also simulated in WRF-CPM but at a slightly faster speed and longer duration. The model realistically represented MCS life cycles. However, the model overestimated the frequency of heavy rainfall but underestimated the amount of rainfall per MCS, probably due to an overestimated number and area of MCSs. It captured the peak time

of MCS well in most of East China, except for a 2-hour delay in the southeast and a failure to reproduce the midnight peak near the Tibetan Plateau. The model also accurately represented the relationship between MCS precipitation and changes in east-west winds with height.

1. Introduction

Mesoscale convective systems (MCSs) are clusters of thunderstorms modulated by mesoscale circulations that encompass contiguous areas of precipitation, typically spanning a spatial scale of at least 100 km (Houze, 2004, 2014). MCSs are a crucial part of global hydrology cycle as they often produce extended and extensive precipitation, contributing significantly to the overall rainfall in tropical and subtropical areas (Feng et al., 2021).

East China lies within the monsoonal belt, marked by recurrent convection due to the convergence of cold and warm air masses, alongside pronounced thermal gradients between land and sea, rendering it a hot spot for MCSs (Cheng et al., 2022; Lu, Tang, et al., 2024; M. Wu & Luo, 2016). This region, densely populated and economically prosperous, stands as the linchpin of China's economic landscape. Consequently, the persistent MCS occurrences and the risk of extreme weather events bear significant ramifications for both regional and national economies.

Researches indicate a rising trend in the frequency and intensity of MCSs during the past 20 years over most areas of eastern China (Guo et al., 2023; Li et al., 2023). Theoretical considerations suggest that precipitation associated with MCSs could potentially intensify and prolong under future warmer climatic conditions, attributed to heightened atmospheric moisture content as indicated by Clausius-Clapeyron scaling (Berg et al., 2013; Tang et al., 2023; Ye et al., 2017). Studies using convection-permitting models indicate that, in mid-latitude regions such as North America, MCSs contribute a higher proportion of total precipitation (Haberlie et al., 2023; Prein et al., 2017). Therefore, it is necessary to conduct reliable model simulation and future projections of MCSs and their related precipitation.

Most general circulation models (GCM) and regional climate models (RCM) with coarse horizontal resolution (100–10km) cannot regenerate MCSs accurately, e.g. coupled model intercomparison Project Phase 6 (Eyring et al., 2016), coordinated regional climate downscaling experiment (Giorgi et al., 2009). The small spatial extents over which convection occurs and the abrupt transitions between intense precipitation and no precipitation might partly be the reason for the limited forecasting accuracy for MCSs (Schumacher & Rasmussen, 2020). Meanwhile, as the coarse resolution models rely on convection parameterization, essential mechanisms, such as cold pools (Houze, 2014), mesoscale circulations (Yang et al., 2017), vertical wind shear (Baidu et al., 2022; Houze., 2004; Richardson, 1999; Weisman & Rotunno, 2004), crucial for MCS genesis and maintenance were not explicitly represented.

Advancements in computing capabilities have facilitated the emergence of regional and global convection-permitting models (CPMs), characterized by finer grid spacing (≤4km), enabling the explicit resolution of crucial aspects of deep convection and eliminating the need for convection parameterization (Lucas-Picher et al., 2021; Rasmussen et al., 2020; Stevens et al., 2024). Regional CPMs have been applied to provide more reliable climate information (Guo et al., 2020; Lucas-Picher et al., 2021; Prein et al., 2015; Rasmussen et al., 2020) and future projections (Klein et al., 2021; Senior et al., 2021). CPMs have demonstrated their capacity to enhance precipitation simulations, particularly in capturing diurnal variations (Guo et al., 2020; Li et al., 2021; Li et al., 2020; Meredith et al., 2021; Ou et al., 2020; Scaff et al., 2020), although they tend to overestimate the amount of precipitation (Yun et al., 2020). Several studies have utilized regional CPMs to investigate MCSs in South Asia, US, and west Africa, revealing their ability to capture various characteristics, including duration, diurnal cycle, and intense precipitation (Berthou et al., 2019; Chen et al., 2022; Prein et al., 2020). To date, there has been limited investigation into the capability of CPMs to simulate MCSs in East China. Existing studies have primarily focused on the evaluation of global (Li, et al., 2023) or regional (Yun et al., 2021) CPMs with horizontal resolutions from 10km to 3km, spanning 4–10 years, in simulating MCSs and their precipitation characteristics. These investigations have revealed that CPMs exhibit reliability in representing the climatological attributes and diurnal cycle of MCS rainfall. However, no regional CPM studies covering the extensive domain of East China over a time period of up to two decades have been conducted. Such long-term simulations are crucial for advancing understanding of MCS mechanisms, as they provide sufficiently large sample sizes for further composite analysis, especially in arid and semi-arid regions where MCSs are relatively infrequent. Therefore, it is imperative to explore whether CPMs can effectively capture the features of MCSs over eastern China in long-term simulations covering a large spatial domain.

Total column water vapor (TCWV) and shear are well-established factors controlling MCS behavior and rainfall. MCS rainfall is indicated to be related to TCWV (Fitzpatrick et al., 2020). Additionally, recent observational studies have demonstrated that wind shear influences rainfall intensities in squall line MCSs (Klein et al., 2021; Long et al., 2023; Senior et al., 2021; Wang et al., 2019). Strong shear tilts convective cells, effectively separating updrafts and downdrafts, which enhances convective activity and increases precipitation intensity. Strong vertical wind shear is often associated with long-lived storms of moderate speed and size, which are characterized by colder brightness temperatures and higher rain rates (Baidu et al., 2022). Idealized Large Eddy Simulation (LES) studies by Mulholland et al., (2021) further reveal that stronger updrafts and reduced entrainment dilution, driven by shear, contribute to these effects on MCSs. Capturing shear effects remains a challenge for CPMs (Senior et al., 2021), highlighting the need for further model development. Recent work by Maybee et al., (2024) demonstrates that while older versions of Met Office Unified Model (UM) failed to simulate shear effects, the latest version successfully captures them. As external forcings, both vertical wind shear and TCWV play a crucial role in shaping the intensity and organization of MCSs by influencing their internal structure and dynamic processes. Therefore, assessing the ability of the WRF-CPM to accurately capture these factors is essential.

This study conducted a 22-year (2000–2021) regional climate simulation with a horizontal resolution of 4km using Weather Research and Forecasting (WRF) model. Additionally, to detect MCSs from model output, the simulated cloud top temperature was computed utilizing the Community Radiative Transfer Model (CRTM) with WRF outputs. The main objective of this study is to investigate the performance of long-term convection-permitting simulation in reproducing MCS, MCS precipitation properties including climatology features, duration, propagation, area, and diurnal cycle, as well as the external forcing, particularly shear effects.

The subsequent sections of the paper are structured as follows. Section 2 describes CPM model configuration, observation datasets, and analysis methods utilized in this study. WRF-CPM simulations of MCS climatology, properties, MCS precipitation features, and associated shear effect are analyzed in section 3. Concluding remarks are given in section 4.

2. Data and Methods

2.1 Observational Data

CPC-4km (Janowiak et al., 2001), which is a satellite-derived IR brightness temperature (Tb) released by the Climate Prediction Center/NCEP/NEWS/NOAA (CPC), was used to identify and track MCSs. The CPC-4km dataset is generated by merging several infrared channels of geostationary meteorological satellites. It covers the global area from 60°S–60°N with a horizontal resolution of 4 km and a temporal resolution of 30 minutes and has undergone viewing angle and parallax corrections. Although the CPC-4km dataset has a high data availability of 97.52% in East Asia, missing data—often referred to as the "satellite puzzle"—can still introduce uncertainties in detecting and tracking MCSs (Teramura et al., 2019). These gaps may arise from satellite maintenance, data transmission issues, and the limitation of satellite coverage. Previously CPC-4km Tb data has been utilized to investigate the climatology and historical trends of MCSs in East China (Cheng et al., 2022; Feng et al., 2021; Y. Guo et al., 2023; Lu, Tang, et al., 2024) by identifying cold clouds related to deep convection.

The merged precipitation data (IMERG, V06B), which is launched by NASA in the Global Precipitation Measurement (GPM) mission, is a multi-satellite derived precipitation retrieval product that provides precipitation estimation at 0.1° × 0.1° horizontal resolution every 30 minutes globally (60°S–60°N). The final product is formed by integrating retrievals from multi-satellite sources, including passive microwave and IR sensors. These retrievals are then merged with estimates obtained from the GPM Core Observatory (Tan et al., 2019). IMERG has drawn much attention and is employed to evaluate MCS precipitation (Chen et al., 2022; Feng et al., 2021; Kukulies et al., 2021) since it might offer the best precipitation estimations (Kidd et al., 2017).

2.2 Model Configuration

The fully compressible and nonhydrostatic WRF model Version 4.3.3 (Skamarock et al., 2019) was used in this study to investigate MCSs and their related precipitation over eastern China. The 31km ERA5 reanalysis (Hersbach et al., 2020) was used as initial and lateral boundary conditions, and was downscaled to the CP scale to generate regional climate model simulation. The bottom boundary conditions were 3-hourly sea surface temperature data (SST) from ERA5, monthly Green Vegetation Fraction (GVF) and Leaf Area Index (LAI) from the original WRF dataset. The model was run on an 840×840 grid with a horizontal resolution of 4km, covering the most area of East China (**Figure 1**) under Lambert projection. The sponge boundary scheme was applied to the model boundaries and buffer zone, which consists of 15 layers. Vertically there are 50 levels, and the model top height is 50 hPa. WRF simulations were conducted for 23 summers since 1999 to 2021, initialized from every 21st May and integrated until 1st September. The first ten days each summer were used as spin-up time.

The physical parameterization schemes chosen are listed in **Table 1**. Specifically, the cumulus convective parameterization was switched off so that the convection features were explicitly resolved. Such choice of physical parameterization scheme follows previous work by Guo et al., (2020, 2022), where CP-resolution WRF simulation was conducted decadal long over eastern China, and its ability of reproducing summer precipitation was evaluated. The turbulence and mixing option was set as 1 (default) which evaluates the second-order diffusion term on coordinate surfaces. The model simulation is named as WRF-CPM hereafter.

Diurnal cycle of total precipitation simulated by WRF-CPM was evaluated by comparing with IMERG V06 and ERA5 (see Supporting Information). Results show that WRF-CPM improves the representation of rainfall diurnal cycle especially in the East of Tibetan Plateau compared to ERA5 (SI, **Figures S1 and S2**).

To generate cloud top temperature of WRF-CPM, the Community Radiative Transfer Model (CRTM, Weng et al., 2005), version 2.3.0, was employed to produce imagery from the Himawari-8 satellite, specifically utilizing the near-infrared channel at 11.2 μm. The three-dimensional variables from WRF-CPM output, including pressure, temperature, water vapor, and the mass mixing ratio of cloud water, rainwater, graupel, snow and ice, and the two-dimensional fields encompassing latitude, longitude, and surface temperature were passed to the CRTM to calculate the cloud top temperature.

2.3 Tracking Method

Observed and simulated MCSs were tracked based on Tb and precipitation by the Object-based Tracking (OT) algorithm (Guo et al., 2022) which identifies cold convective clouds through Tb and also includes a process to calculate the precipitation feature (PF) of potential MCSs.

The WRF-CPM output and CPC-4km Tb data were initially upscaled to an 8 km horizontal resolution by averaging values from all grids within an 8 km radius of each grid point (Clark et al., 2014), then conducting a Gaussian filter on a 3×3 window. The sensitivity test on the smoothing window (not shown) indicates that the selected smoothing procedure is able to mitigate oversegmentation and eliminate small-scale signals, thereby enhancing the identification of mesoscale systems, while it still retains details in the high-resolution model simulation. To align with the upscaled Tb and precipitation data, IMERG was also interpolated onto the 8 km grid.

In this study, we define an MCS as a convective system with:

(1) Cold cloud system (CCS) with Tb ≤- 32℃, area≥ 40,000 km^2;

(2) Convection core with Tb ≤ -52℃, area ≥ 30,000 km^2 embedded in CCS;

(3) A PF with rain rate ≥ 2mm/h, major axis > 100km in convection core;

(4) Both (1) and (2) last for at least 3 hours, and (3) lasts for longer than 2 hours continuously.

Such a definition follows Feng et al., (2021), Houze, (2018), and Yang et al., (2015). The threshold values of cloud top temperature, cloud areas, and PF were selected based on tests over the Yangtze-Huaihe River basin in eastern China, where we compared climatology and properties of MCSs derived from CPC-4km Tb data using IMERG or radar reflectivity as PF. For more details, see Lu et al. (2024).

The MCSs were identified and tracked through five steps (SI, Figure S1). Initially, regions meeting value and area thresholds at each time step are designated as convective cores during the identification phase. Subsequently, each convective core is expanded outward, pixel by pixel, to encompass contiguous areas exhibiting warmer cloud top temperatures, thereby forming potential stratiform clouds and were marked as cold cloud. In the third step, precipitation areas with contiguous rainy area ≥ 2mm/h within each cold cloud with major axis ≥ 100 km are identified as PFs. The fourth step employs the area overlapping method in the OT algorithm to connect cold clouds across successive time steps. If two cold clouds overlap for more than 50% of areas in two successive time steps, they are considered part of the same potential MCS. Tracking continues until the cold cloud areas no longer meet the 50% overlapping area criteria. Finally, all potential MCS duration and PF duration are assessed to identify those exceeding the time criteria. The potential MCSs that meet the duration selection criteria are labeled as MCS_1, MCS_2, ..., MCS_N, where N represents the total number of MCSs traced.

2.4 Analysis methods

In this study, we first identified, tracked, and labeled MCSs within the region of interest at each time-step (1-h time intervals). Using the mask files of all identified MCSs, we generated a corresponding MCS precipitation dataset.

The probability density function (PDF) of MCS precipitation on each pixel was calculated as the ratio of the number of MCS precipitation pixels within each bin to the total number of pixels (time steps×grid points). The distribution of MCS contributions to total precipitation was determined as the fraction of total MCS precipitation to total precipitation within each bin. Additionally, the PDF for each MCS was calculated based on its areal hourly average precipitation, derived by dividing total precipitation by the hourly average area and duration of each MCS.

At each MCS time step, the mass centroid of convection cores was tracked to determine propagation speed, track length, and direction. To analyze the relationship between MCS propagation and mean flow, we used the complex correlation coefficient method (Kundu, 1976) to assess the correlation of MCS propagation and mean flow, accounting for both direction and speed.

Here, we flatten the 2 dimensional u, v components of 22-year JJA average mean flow and MCS propagation to 1D representation, and define the horizontal velocity vector at pixel k as:

$$w(k) = u(k) + iv(k) \tag{1}$$

where $i = \sqrt{-1}$.

The complex correlation coefficient between mean flow (w_1) and MCS (w_2) is their normalized inner product:

$$\rho = \frac{\overline{w_1^*(k)w_2^*(k)}}{\sqrt{\overline{w_1^*(k)w_1(k)}}\sqrt{\overline{w_2^*(k)w_2(k)}}} \tag{2}$$

Here, the asterisk (*) indicates the complex conjugate, and the bars indicate arithmetic mean. ρ is a complex number where the magnitude represents the overall correlation strength (hereinafter CORR) and the phase angle indicates the average counterclockwise angle of w_2 with respect to w_1.

In terms of the east-north components, (2) can be expanded as:

$$\rho = \frac{\overline{u_1u_2+v_1v_2}}{\sqrt{\overline{u_1^2+v_1^2}}\sqrt{\overline{u_2^2+v_2^2}}} + i\frac{\overline{u_1v_2-u_2v_1}}{\sqrt{\overline{u_1^2+v_1^2}}\sqrt{\overline{u_2^2+v_2^2}}} \tag{3}$$

The phase angle is:

$$\alpha = tan^{-1} \frac{\overline{u_1 v_2 - v_1 u_2}}{\overline{u_1 u_2 - v_1 v_2}} \quad (4)$$

3. Results

3.1 MCS spatial distributions

The spatial distributions of annual average MCS numbers, annual total rain rate of MCSs, and their contribution to total precipitation from observation (CPC-4km and IMERG) and WRF-CPM, and their differences in JJA during 2000–2001 are illustrated in **Figure 2**. During the summer season, the coastal region in southwest China experiences the highest frequency of MCSs, peaking at approximately 45 per year (**Fig. 2**a). This frequency exhibits a southwest-to-northeast decreasing gradient. Additionally, a significant number of MCSs, approximately 30 per year, are observed to the east of the Tibetan Plateau. MCSs are notably infrequent in northern China, particularly in regions such as northeastern China and northwestern China, where MCS occurrences are nearly absent (**Fig. 2**a). The WRF-CPM model accurately represents these spatial characteristics over land; however, it tends to overestimate precipitation over most region of East China (**Fig. 2**e). Specifically, notable overestimation can be observed in regions such as the southeast of the Yungui Plateau, the eastern coastal areas, and northeastern China (**Fig. 2**c). Moreover, WRF-CPM generates fewer MCSs in east Tibetan Plateau. The underestimation of MCSs in the ocean near the southern boundary of WRF-CPM is pronounced, primarily due to the distinct boundaries between the CPC-4km and WRF-CPM in this area. To assess whether the southern boundary of the model domain strongly affects oceanic MCSs and subsequently influences MCSs over land through propagation, we analyzed MCS propagation in the sea-land transition along the South China Sea coastline (not shown). The results indicate that the southern boundary exerts a limited impact on land-based MCSs. This is primarily because the southern boundary is located approximately five degrees of latitude from the coastline, making it challenging for MCSs originating near the southern model boundary to propagate into the main study area.

The observed distribution of MCS rainfall is similar to that of MCS numbers across mainland China (**Fig. 2**d). The highest rain rates, surpassing 360 mm/year, are concentrated in the southwestern coastal area of China. In the eastern region of the Sichuan basin, MCS rain rate is notably elevated, reaching 340 mm/year. In these areas, MCSs account for at least 35% of total precipitation (**Fig. 2**g). Additionally, a considerable amount of MCS precipitation is recorded along the eastern coast of China, amounting to 180 mm/year (**Fig. 2**d), with MCS precipitation contribution to 25% of the total precipitation in the region (**Fig. 2**g). Compared to the deep tropical areas, where MCSs account for over 50–70% of total precipitation (Zhao, 2022), their contribution in eastern China is relatively smaller. MCSs in East China occur less frequently than those embedded in the Intertropical Convergence Zone (ITCZ). Moreover, the lower MCS contribution observed in our study, compared to previous work focusing on mid-latitudinal MCSs (Feng et al. 2021; Li et al. 2020; Yun et al. 2021), primarily stem from the stricter threshold on convective-core area. The simulated MCS rain rate (**Fig. 2**e) and MCS precipitation contribution (**Fig. 2**h) by WRF-CPM exhibit patterns similar to the observed data. However, there is a notable overestimation of MCS rain rate observed in the hotspot regions of MCS precipitation, exceeding 300 mm/year, as well as in northeastern China where it reaches around 50 mm/year (**Fig. 2**f). This discrepancy corresponds to the areas where there is an overestimation of MCS numbers. A positive bias in the contribution of MCS precipitation is evident in southwestern regions, although a larger area of overestimation is observed in the eastern and northeastern parts of China, exceeding the observations by approximately 12% (**Fig. 2**i). Conversely, notable underestimation is observed in the eastern Tibetan Plateau, with a deviation of around -16% (**Fig. 2**i).

Since atmospheric instability and water vapor are essential for MCS formation, we examined the 22-year average summer CAPE and TCWV distributions from ERA5 and WRF-CPM (**Figure 3**). ERA5 data show a decrease in TCWV across China from east to west and south to north. In the third-step terrain, TCWV averages ~55 kg/m^2, decreasing northward to ~30 kg/m^2. The second-step terrain sees further declines to ~20–30 kg/m^2, except in the Sichuan Basin, where TCWV is higher due to topography-related water vapor sink effect. Northwest China has the lowest TCWV, around ~10 kg/m^2. TCWV over South China Sea and Indochina Peninsula is higher than that in China mainland (**Fig. 3**b).

CAPE, a measure of atmospheric instability, also decreases from southeast to northwest. Southeastern coastal areas average ~1300 J/kg, peaking at nearly 2000 J/kg along the South China Sea coast. Additionally, there is a band of high CAPE values (~2300 J/kg) in the lower reaches of the Yangtze River, which is related to the quasi-stationary Meiyu front that persist in this region during summer. An extreme high value of CAPE reaching to ~2300 J/kg exists in South China sea.

With the low-level southwest monsoonal air-flow, instable warm and moist air is transported from the ocean to land area of China, providing favorable conditions for the activity of MCSs in summer (**Fig. 3**e).

Overall, the WRF-CPM tends to overestimate CAPE across most regions except northwest China (**Figs. 3**d, f), corresponding to an overestimation of MCS numbers. The model also overestimates TCWV in southern coastal areas, the second-step terrain east of the TP, and northeastern China (**Figs. 3**a, c), leading to an overestimation of MCS precipitation in these regions.

3.2 MCS propagation

Figure 4 displays the 22-year spatial patterns of duration, propagation speed, and propagation direction of MCSs in East China from both CPC-4km and WRF-CPM simulations. Median values are displayed to minimize the influence of outliers on the statistical results. Because this study focuses on land-based MCSs, data over the ocean were excluded. Observationally, the MCS duration spans at least 3 hours across most regions in East China, with the longest durations observed in the southwest coastal area, reaching around 9 hours (**Fig. 4**a). Regions situated in the middle of China, east of the plateau, exhibit longer MCS durations compared to their surroundings (**Fig. 4**a). The spatial pattern of MCS duration from WRF-CPM closely resembles that from CPC-4km (**Fig. 4**b). In eastern China, the duration of MCSs simulated by WRF-CPM is, on average, one hour longer than that of CPC-4km MCSs, except in the eastern Tibetan Plateau, where simulated MCSs duration is approximately 3 hours shorter (**Fig. 4**c).

The observed MCS speeds vary across East China, ranging from around 10 m/s in the Sichuan Basin, gradually increasing to 14 m/s in the southeastern area and 20 m/s in the northeastern China (**Fig. 4**d). The combination of long durations and slow speeds in the Sichuan Basin and southwestern coastal areas leads to prolonged MCS rainfall, explaining the high MCS rain rate and contribution of MCS rainfall to total precipitation in these regions (**Figs. 4**d and g). The WRF-CPM simulation captures the spatial distribution of speed well with a spatial correlation coefficient at 0.86 (**Fig. 4**e). Speeds are simulated faster in a wide range of area especially in north China for up to 5 m/s. MCSs are reproduced slower in lower-reach of Yangtze River, northeast China and the north to Sichuan Basin (**Fig. 4**f).

In general, most MCSs in China propagate southeasterly (**Fig. 4**g). MCSs in southern China and East Tibetan Plateau tend to move more southerly, while those in the YRB and northeastern China exhibit more easterly movement (**Fig. 4**g). WRF-CPM captures the spatial distribution of MCS propagation direction well with a correlation coefficient of 0.86. The WRF-CPM simulation reproduces the southerly movement of MCSs in southern China and the easterly propagation in the YRB and northeastern China (**Fig. 4**h), but simulates easterly propagation of MCSs near Sichuan basin and north China (**Fig. 4**i).

Another question we explore is the influence of mean flow on MCS propagation. We examined the relationship between MCS propagation speed and direction and the wind fields at 200 hPa, as well as the 500–850 hPa wind shear (**Figs. 4**g, h). Quantitatively, the correlation between MCS propagation and the 200hPa wind is strong, with a complex correlation coefficient of 0.76 and a clockwise shift of 1.05º. This is followed by a correlation of 0.72 with 500–850hPa wind shear, showing a counterclockwise shift of 4.08º (**Table 2**). A high correlation of 0.62 is also observed with 500hPa winds. These results highlight the critical role of upper-level winds, mid-level winds, and deep wind shear in influencing MCS propagation.

The WRF-CPM model shows a higher correlation coefficient than ERA5, indicating that while simulated MCSs do not perfectly match satellite observations, WRF-CPM effectively captures the response of convection to wind and background fields. The mean flow between WRF-CPM and ERA5 are subtle, as WRF-CPM uses ERA5 for initial and boundary conditions. Analyzing biases in MCS propagation from mean flow is challenging, some trends are evident. For example, faster MCSs in southwestern China might result from a southeasterly bias in 200hPa winds, while counterclockwise propagation biases in central-northern China may be linked to a westward wind bias at 200hPa. Additionally, as a terrain-transition region, complex topography gradients pose challenges for models in representing planetary boundary layer (PBL) processes that alter convection organization and propagation (Kukulies et al., 2023; Ma et al., 2024). In YHR, the northwestward shift and slower MCS speeds are associated with wind shear biases, and the upper-level convergence bias associated with a cyclonic circulation bias at 200hPa, which decreases upward motion and slows MCS propagation. The direction bias in northeastern China may stem from a significant difference in the number of MCSs detected in simulations (390) versus observations (86), with WRF-CPM producing more locally initiated MCSs due to overestimated moisture and instability in this region (**Figure 3**). The variation in propagation direction, influenced by subtle differences in circulation patterns compared to ERA5, may reflect biases in WRF-CPM's storm response to the background circulation.

Yet in different regions, the driving factors vary. In southwest China, upper-level winds are key (Zhang et al., 2025). In southeast China, land-sea circulation, deep-layer wind shear, lower-level monsoonal flows, moisture transport, and CAPE also play important roles (Wang et al., 2024). In the Yangtze-Huaihe River basin, factors like the low-level jet, vertical wind shear, stable nocturnal boundary layer, evaporative cooling and cold outflows affect quasi-stationary MCSs (Zhao et al., 2020). The dynamics of MCS propagation and the possible processes leading to the model behavior is worth a deeper and more systematic investigation by conducting more detailed analysis such as composite analysis in the future.

3.3 MCS properties

To enhance our comprehension of the pattern of simulated MCS rainfall bias, the probability density function (PDF) and cumulative distribution function (CDF) of MCS precipitation for every pixel over 6 sub-regions are depicted in **Figure 5**. In each of the six regions, WRF-CPM indicates an underestimation of the probability for light and moderate MCS rainfall, particular below 12mm/h in ETP, YRB, SEC, and NEC (**Figs .5**a, b, c, e), and under 15mm/h in NC and NWC (**Figs .5**d, f). Conversely, WRF-CPM exhibits substantial overestimation of the probability for extreme MCS precipitation across all six sub-regions (**Figs .5**a–f). Consequently, in IMERG, moderate and light rainfall contributes more to the total MCS precipitation compared to WRF-CPM, while the reverse is observed for extreme rainfall (**Figs .5**g–l). Therefore, it is the overestimation of precipitation surpassing approximately 15mm/h on each pixel that results in the overall overestimation of total MCS rainfall as portrayed in **Fig .5**f.

Aside from examining the spatial characteristics of MCSs and frequency distributions of hourly pixel MCS rainfall, the temporal evolution of MCS properties is also investigated. The lifetime of each individual MCS is divided into 10 normalized life stages, following the method outlined in (Bouniol et al., 2016), where stage 1 signifies initiation and stage 10 represents system dissipation. This division is achieved by linearly interpolating the original values. **Figure 6** illustrates the relationship between MCS area, average rain rate, total precipitation, and the areal average cloud top temperature of MCS convective cores throughout their normalized life cycle.

The cloud top temperature of MCS convective cores reaches its lowest point at stage 2 in both observation and WRF-CPM simulation, gradually rising towards the dissipation stage (**Figs.**

6a and c). The areal average core precipitation is the most intense when an MCS is detected, peaking at stage 1, diminishing gradually as the MCS evolves (**Fig. 6**a). The average MCS precipitation (including the stratiform areas) is highest at stage 2 (**Fig. 6**c). Generally, WRF-CPM produces colder convective cores compared to satellite observations. The convective area expands, reaching its peak at stage 5 (**Fig. 6**b), after which stratiform clouds begin to grow until stage 7. Convective clouds decay more quickly than stratiform clouds. The areal total rain rate of convective cores exhibits a similar evolution to that the convection areas (**Fig. 6**b). The observed CCS area peaks at stage 7, with the total precipitation the largest at stage 5. Following stage 5, the total rainfall of the MCS decreases at a faster pace than the decline in MCS area (**Fig. 6**d). While WRF-CPM generates larger MCSs (**Figs. 6**b, d), the total rain rate is smaller (**Figs. 6**b, d). Consequently, the average rain rate of convective cores is also lower in WRF-CPM (**Figs. 6**a, c). The bias may stem from the underestimated WRF-CPM cloud top temperature generated by CRTM, causing MCSs in the model to appear larger than those in satellite observations. This leads to lower average precipitation per pixel in the simulated MCSs compared to the observed ones.

From **Figure 2** and **Figure 5**, it is evident that the total precipitation attributed to MCS is overestimated, primarily due to an excessive contribution from extreme precipitation pixels. However, **Figure 6** reveals that both the areal average and total precipitation of MCS is smaller in the WRF-CPM simulation compared to satellite data. To gain deeper insights into the structure of MCS precipitation, another MCS precipitation PDF from aspects of each MCS across 6 sub-regions is represented in **Figure 7**. Unlike **Figure 5** which illustrates MCS precipitation probability distribution from the perspective of pixels, here the samples are the hourly areal average precipitation for each MCS. Generally, the probability of observed MCS average rainfall peaks at around 3 mm/h, with probabilities ranging from 22.4% to 40% (indicated by pink lines). WRF-CPM exhibits peaks shifting the left, centered around 2 mm/h with higher probability. Furthermore, satellite data shows a larger probability on larger precipitation bins than WRF-CPM. However, analysis of the sample counts of MCSs indicates that WRF-CPM tends to generate an excessive number of MCSs in most regions, except for the NWC. Meanwhile, the average area of MCSs is larger in WRF-CPM simulation (**Figs. 6**b, d). These discrepancies imply that while satellite-derived MCSs exhibit more intense rainfall compared to model-simulated ones, WRF-CPM generates an excessive number of MCSs, leading to an overestimation of total MCS rainfall in the model.

To understand the long-term properties of MCSs in East China and evaluate CPM's ability to capture the features, **Figure 8** shows the violin plot of average convection core areas, propagation speed, CCS area, duration, propagation distance, mean and total convective precipitation, mean and total CCS precipitation in 6 subregions. Violin plots offer a visual representation of data distribution through density curves. The width of each curve represents the approximate frequency of data points with each value bins.

In general, WRF-CPM captures the features of MCSs across all six sub-regions, albeit with some discernible biases. Observed convection core areas exhibit a median value of approximately 8,000 km^2 (**Fig. 8**a), while CCS areas have a median value of around 20,000 km^2 (**Fig. 8**c). Notably, WRF-CPM tends to generate larger MCSs, particularly evident in SEC and NWC. In NC, while WRF-CPM produces MCSs with smaller core areas, it yields larger CCS areas. Conversely, in YRB and NEC, WRF-CPM simulates smaller CCSs. The behavior that WRF-CPM produces MCS with larger CCS but smaller convective cores may stem from CPMs' tendency to generate smaller but more intense precipitation events (Prein et al., 2013). During summer, CPMs often underestimate the area of convective clouds (Prein et al., 2015). Additionally, we assume that the microphysics scheme used in this study (WSM5) appears to contribute to these biases. The scheme tends to produce insufficient cloud water in the mid and lower levels while generating excessive rain water especially at upper level (Guo et al., 2019), resulting in smaller convective clouds. Simultaneously, the enhanced cooling effect in the upper levels could promote the formation of larger cold cloud areas, leading to an overestimation of stratiform cloud coverage. In most regions, WRF-CPM exhibits a tendency to generate MCSs that propagate at faster speeds (**Fig. 8**b) and endure for longer duration (**Fig. 8**d). However, in YRB, the distribution of propagation speeds is skewed towards slower values (**Fig. 8**b), likely due to biases in the slight mid- and lower-level wind shear simulated by WRF-CPM, which is incorrectly oriented toward the west and southwest. Consequently, MCSs simulated by WRF-CPM travel longer distances, with a greater portion falling within longer track length value bins, except in YRB where track length is more concentrated in shorter bins (**Fig. 8**e). The observed average pixel core precipitation demonstrates median values ranging from 2.5 mm/h in NWC to 5 mm/h in NC (**Fig. 8**f), while CCS precipitation exhibits median values ranging from 1.8 mm/h in NWC to 3.8 mm/h in NC (**Fig. 8**h).Moreover, observed total core precipitation displays median values ranging from 15,000mm in NWC to 21,000 mm in NC (**Fig. 8**g). The median values of total CCS precipitation hovers around 25,000 mm, except in NC where it is approximately 30,000 mm. In comparison to satellite data, MCS precipitation simulated by WRF-CPM shows a more concentrated distribution around the medium (25th percentile) value for pixel-average (total) precipitation, for both core rainfall and CCS rainfall. Additionally, although WRF-CPM underestimates the average MCS precipitation amount across all six sub-regions, its overestimation of both the number of MCSs and CCS areas leads to an overestimation of the spatial distribution MCS precipitation, as shown in **Figure 2**.

3.4 Diurnal cycle

To depict the spatial and temporal variability of MCS precipitation in eastern China, **Figure 9** illustrates the diurnal cycles (shown as Beijing Time, BJT) of annual-mean accumulated precipitation amounts for six sub-regions, presented as a function of longitude. The precipitation is averaged in latitude and summed in longitude. The MCS precipitation exhibits eastward propagation across all six domains, consistent with previous analyses indicating predominantly eastward movement in MCSs. Two peaks in longitudinal total precipitation are observed in SEC, with one starting from 105°E starting after 1800 BJT and the other to the east of 110°E starting from early morning. Nocturnal rainfall originates from the southeast of TP and then moves eastward. In the afternoon, MCS rainfall begins to develop over plain areas. This phenomena is consistent with the data shown in **Fig. 9**a and aligns with findings from previous study (Chen et al., 2009; Liu et al., 2021). Notably, MCS rainfall also starts in the coastal region east of 115°E from early morning after 0400 BJT. The early-morning rainfall is likely triggered by the convergence of land-sea breeze (Dong et al., 2023). In most regions, the diurnal peak of MCS total precipitation occurs at night, typically around 1800–2000 BJT (**Figs. 9**f, j, n, q, v), except in ETP (**Fig. 9**b). Additionally, another is observed in the early morning, around 0300 BJT, in regions including ETP (**Fig. 9**b), YRB (**Fig. 9**f) and SEC (**Fig. 9**j). Overall, the WRF-CPM model captures the eastward propagation trend and longitudinal peak locations of total MCS precipitation, although displaying biases in peak timing and rainfall area ranges compared to observations (**Figs. 9**c, g, k, o, s, w). For instance, in ETP, the model exhibits a rain peak area for midnight rainfall shifted 1° eastward compared to CPC-4km, and a false signal at 1800 BJT to the east of 107.5°E (**Fig. 9**c). WRF-CPM reproduces the morning peak in YRB but misinterprets its location, overestimating MCS precipitation around 118°E. Meanwhile, WRF-CPM simulates continuous rainfall from 2100 BJT to 0900 BJT around 103°E, where the propagation of MCS rainfall is weaker than observed (**Fig. 9**b). Similar eastward biases are evident in YRB (**Fig. 9**g) and NWC

(**Fig. 9**w). Additionally, in SEC, the west rain peak propagates for a longer duration, extending until 1700 BJT, which is 3 hours longer than observed in CPC-4km (**Fig. 9**k). The WRF-CPM overestimates both the magnitude of MCS precipitation and amplitude of its diurnal cycle in NEC (**Fig. 8**o), where simulated total MCS precipitation is approximately 1.5 times the observed. This discrepancy may be attributed to the model's strong overestimation of MCS numbers in NEC.

Figure 10 presents a comparison of the spatial distribution of diurnal peak time for 22-year JJA MCS initiation and maturation numbers derived from CPC-4km and WRF-CPM simulation. The topography, represented by contour lines at elevations of 4,000m, 2,000m, and 600m, is also depicted. Pixels with fewer than 5 MCSs are treated as missing values. The peak time for MCS initiation exhibits some relationship with topography and distance from the ocean. In the eastern part of China, where altitudes are below 600m, the initiation peak typically occurs in the late afternoon around 1700 LST, progressing to later hours further north, reaching nightfall around 1900 LST (**Fig. 10**a). In regions with intermediate topography, ranging from 600m to 2,000m in the central part of China, the majority of areas experience initiation peaks during the night around 2000 LST, with basin areas to the east of the plateau (Sichuan Basin) showing even later peaks around midnight (**Fig. 10**a). Such midnight storm peak might be related to the diurnal cycle of low-level jets which are enhanced in the midnight, and the diurnal variation of temperature advection from Tibetan Plateau (Chen et al., 2010). Warm and moist mid-level advection from the Tibetan Plateau suppresses the initiation of afternoon thermal convection by stabilizing the troposphere. Reduced warm mid-level advection allows the release of accumulated low-level unstable energy, favoring nocturnal rainfall. Meanwhile, enhanced low-level moisture flux convergence and warm advection from lower latitudes due to the intensified nighttime low-level jet creates an environment conducive to the initiation of MCSs (Li et al., 2024; Li et al., 2024; Wu & Li, 2023). The WRF-CPM model generally captures the midnight peak, albeit with an advancement of approximately 2 hours. In the East of Tibetan Plateau, where elevations exceed 4,000m, MCSs are predominantly detected in the afternoon around 1700 LST (**Fig. 10**a). The maturation peak typically occurs 1 to 3 hours later than the initiation peak (**Fig. 10**g).

The diurnal peak patterns derived from WRF-CPM simulations closely resemble those of CPC-4km, particularly in the eastern part of China, with the exception of a one-hour later peak observed in southeastern China. However, in the central regions of China, WRF-CPM simulation fails to capture the early-morning peak. Instead, it generates an afternoon peak (**Fig. 10**b).

Analyzing the disparities between CPC-4km and WRF-CPM, the most significant advancement in initiation peak timing is observed in regions with intermediate topography between 4,000 m and 2,000 m, where the advancement can exceed 6 hours (**Fig. 10**c). In regions with steep topography gradients, strong surface heating combined with monsoonal circulation drives nocturnal convection. The convergence of cold downhill winds from radiatively cooled mountains and warm, moist monsoonal wind creates a favorable environment for convection to initiate (Karki et al., 2017). WRF-CPM might struggle to accurately capture the diurnal variation of thermal characteristics related to complex topography, which can affect its representation of MCS precipitation. **Figure S4** illustrates that WRF-CPM indeed produces an early-morning peak with total MCS rainfall of approximately 100 mm, which is around 50 mm less than that derived from satellite observations. Additionally, a larger peak is generated in the afternoon, with total MCS precipitation reaching around 130 mm at 1800 BJT, coinciding with the period when the MCS total rainfall is the smallest in satellite data. A further analysis of the diurnal cycle of low-level (850hPa) temperature reveals that WRF-CPM exhibits a quicker thermal response to solar radiation, with earlier heating from 0600 BJT and cooling from 1800 BJT over steep topography between the first- and second-step topography (not shown). Although it is challenging to confirm whether WRF-CPM simulates the radiation or land-atmosphere response in these regions wrongly—given that ERA5 results at 850 hPa are not entirely realistic—we hypothesize that this quicker thermal response fosters more favourable conditions for convection in adjacent regions. Consequently, this could lead to an earlier peak in the MCS diurnal cycle over second-step topography, further potentially affecting downwind regions to the east.

3.5 Shear effect

Figure 11 illustrates the relationship between average maximum precipitation and 600–925 hPa wind shear, as well as TCWV, for MCSs detected in CPC-4km and WRF-CPM. The wind shear and TCWV data are sourced from ERA5 for observed MCSs. Wind shear was estimated as the averaged shear within the MCSs. It is observed that the average maximum rain rate of MCSs within the same TCWV bins generally increases following the rise in zonal wind shear (**Fig. 11**a). Additionally, all MCSs detected by satellite were accompanied by an average TCWV exceeding 10 kg/m^2. The increase in TCWV results in higher MCS maximum rain rates when wind shear is strong (**Fig. 11**a). The WRF-CPM simulation generally reproduces this feature (**Fig. 11**b). Notably, in the WRF-CPM model, no MCSs are detected when both wind shear and low-level specific humidity are low. The minimum TCWV of simulated MCSs is above 20 kg/m^2, occurring when wind shear exceeds 12 m/s, and the requirement for water vapor becomes more stringent as wind shear decreases. The heatmaps differ because WRF-CPM does not track precisely the same MCSs as those observed by satellite, resulting in variation in the number of MCSs per bin between WRF-CPM and ERA5. Moreover, satellite-derived MCSs may not fully align with the circulation conditions in ERA5. Despite these discrepancies, a correlation coefficient of 0.65 between ERA5 and WRF-CPM heatmaps indicates that WRF-CPM effectively reproduces the overall features among wind shear, TCWV, and maximum MCS precipitation. In particular, WRF-CPM captures the trend that, within the same TCWV bins, the maximum MCS rain rate increases with zonal wind shear, and within the same zonal wind shear bins, the rain rate increases with TCWV.

4. Discussion and Summary

Mesoscale convective systems play a vital role in the global hydrological cycle and are associated with frequent high-impact weather events. Coarse-resolution models struggle to capture MCSs due to their large scales, which prevent the accurate representation of convection's spatial extents of convection and the abrupt transitions between intense precipitation and no precipitation. Furthermore, these models rely on convection parameterizations that cannot explicitly resolve key mechanisms, such as vertical wind shear, cold pools, and mesoscale circulations. This study conducted a long-term convection-permitting (CP) simulation spanning 22 summers from 2000 to 2021 in eastern China. An object-tracking algorithm was utilized to analyze the MCS climatology and assess the CP model's capability to capture MCSs in this region. The results are summarized as follows:

In summer, MCSs are prevalent across eastern China, with the highest frequency observed in the coastal regions of southwest China, displaying a southwest-to-northeast decreasing gradient. MCS rainfall distribution mirrors that of MCS hours, concentrated in the southwestern coastal area, where MCSs contribute to at least 20% of total summer precipitation. The Yangtze-huaihe River basin (YRB) also experiences considerable MCS rainfall, accounting for about 15% of total precipitation. The WRF-CPM generally overestimates MCS frequency, MCS precipitation, and its contribution to total summer rainfall across most area of eastern China, except of the eastern Tibetan Plateau. This overestimation is consistent with previous studies reporting excessive mean precipitation in convection-permitting models (Berthou et al., 2019; Guo et al., 2020; Kendon et al., 2019; Yun et al., 2021). Further analysis on TCWV and CAPE highlights their key roles in supporting MCS activity. WRF-CPM tends to overestimate both CAPE and TCWV in regions, such as northeastern China, where it also overestimates MCS numbers and precipitation.

The 22-year average spatial distribution of MCS duration, propagation speed, and direction in East China shows MCS durations of at least 6 hours in most regions, with the southwest coastal area reaching up to 12 hours. WRF-CPM simulations generally produces longer durations, particularly in the central and northeastern China, by over 3 hours. MCS propagation speeds range from 20 m/s in the East TP and to 12 m/s the Sichuan Basin, increasing to 16 m/s in the southeast. WRF-CPM accurately reflects the spatial distribution of speeds but shows faster speeds by approximately 2 m/s in most regions, except for slower speeds in central and southeastern China. Most MCSs propagate southeasterly, with some moving southerly in southern China and the East TP, and easterly in the YRB and northeastern China. The WRF-CPM simulates these patterns well but with a slight easterly bias.

Average upper-level winds (200hPa), mid-level winds (500hPa), and deep wind shear (500–850hPa), exhibit strong correlation with MCS propagation. Although the WRF-CPM model exhibits biases in the simulation of MCS, it demonstrates a relatively accurate convection response to large-scale wind fields. Region-specific factors, including land-sea circulation, monsoonal flow, and vertical wind shear, further modulate MCS propagation, underscoring the need for more detailed investigations into these dynamics.

The probability density function (PDF) of hourly pixel MCS rainfall reveal that the overestimation of total MCS rainfall is primarily attributed to the overestimation of extreme rainfall on each grid. Analysis of MCS properties, based on their normalized life cycle (stages 1 to 10) indicates that MCSs in eastern China reach their coldest cloud top temperature and maximum convection core precipitation at stage 2, near the initiation stage. The area of MCSs peaks near the middle of the life cycle, close to the dissipating stage. While the WRF-CPM captures this life cycle evolution, it tends to generate colder cloud top temperatures, larger cloud areas, and smaller MCS rainfall compared to observations.

The PDFs of hourly areal average precipitation for each MCS reveal that the probability of average MCS rainfall peaks around 3.5mm/h, with a 10% probability. However, WRF-CPM shifts its peak to the left, around 2 mm/h, with higher probabilities, indicating that WRF-CPM tends to simulate insufficient rainfall. The bias of overestimating total MCS rainfall, despite underestimating average MCS precipitation, is likely due to the overestimation of MCS counts and their area.

WRF-CPM generally performs well in simulating MCS properties, including area, propagation speed, track length, duration, and rainfall, albeit with some noticeable biases. MCS areas are typically overestimated by WRF-CPM, except in the YRB and Northeast China (NEC). Additionally, MCSs simulated by WRF-CPM tend to travel at faster speeds and persist for longer duration, resulting in longer track lengths, except in YRB. However, the observed MCS precipitation is generally underestimated by WRF-CPM, with the distribution being more concentrated between median and 25th percentile values.

MCS precipitation exhibits distinct diurnal features, characterized by eastward propagation across all six sub-regions, consistent with the eastward propagation direction of MCSs. In most regions, the diurnal peak of MCS precipitation occurs in the late afternoon or at night, typically around 1800–2000 LST. Additionally, an early-morning peak can also be observed, especially in the East Tibetan Plateau (ETP). Overall, WRF-CPM effectively captures the eastward propagation trend and longitudinal peak location of MCS precipitation. However, some deviations are noted, such as the eastward shift of rain peak in ETP and NWC, as well as the longer propagation observed in SEC.

The spatial distribution of diurnal peak timing of 22-year summer MCS initiation and maturation reveals a relationship with topography and distance from the ocean. An afternoon peak is prevalent in the eastern part of China on plain areas near the ocean, occurring around 1700 LST, progressing to later hours further north to around 1800 LST. A midnight to early-morning peak can be observed in intermediate topography east of the Tibetan Plateau, occurring from 2000 LST to 0300 LST. Over the Tibetan Plateau, MCSs typically initiate in the afternoon at around 1700 LST, with maturation typically occurring 1–3 hours after the initiation peak.

Although the 4 km WRF-CPM improves the simulation of the diurnal cycle compared to the driving ERA5 dataset, some biases remain. WRF-CPM captures the diurnal pattern well, particularly in eastern China, though it shows a one-hour later peak in the southeastern area. However, the early-morning peak in central northern China is not captured; instead, an afternoon peak appears. Further analysis reveals that while WRF-CPM generates an early-morning peak, it also simulates a false strong afternoon peak. Therefore, the diurnal peak shifts earlier, especially over the second-step topography. Such bias might stem from WRF-CPM's limited ability to capture the thermal diurnal variation related to complex topography (Jeworrek et al., 2021; Liu et al., 2022; Ma et al., 2022), where the convergence of cold downhill winds from a radiatively cooled high mountains with warm-moist monsoonal wind triggers nocturnal convection. leading to an earlier onset of favorable conditions for convection, particularly near steep topography. Additionally, boundary layer, radiation, and land-surface parameterizations may still affect local thermodynamic and dynamic processes, influencing the diurnal cycle of convection genesis (Cintineo et al., 2014; Halladay et al., 2024; Lipzig et al., 2023). Further investigation is needed to understand this process in detail.

Analysis based on ERA5 shows that summer MCS in East China exhibit a relationship with vertical wind shear and TCWV. As wind shear and humidity intensify, the maximum rain rate of MCS increases. This study is the first to demonstrate that the WRF-CPM can also replicate these effects, confirming its capability to simulate convection system response to the background circulation.

This study presents the most extensive convection-permitting regional climate model simulation in eastern China to date, boasting the highest spatial resolution, longest coverage time, and broadest spatial extent. The model's capability in capturing MCSs, MCS precipitation, the MCS diurnal cycle, and other relevant features has been confirmed through the evaluation. Moreover, our study is the first to show that WRF model can capture shear effects controlling MCS behavior and rainfall, indicating the model's capability to simulate MCS dynamics. The demonstrated effectiveness of these simulations underscores their potential reliability and value in further investigations into regional climate changes and their impacts. With its extensive temporal and spatial coverage, the simulation offers ample data for conducting further analysis of MCS mechanisms.

Acknowledgments

This work was funded by the National Key Research and Development Program of China (grant no. 2023YFF0805404). The numerical calculations presented in this paper were performed on the supercomputing facilities at the High-Performance Computing Center (HPCC) of Nanjing University. The authors extend their gratitude to the ECMWF for providing the ERA5 reanalysis data used to drive the CP simulation and evaluate background circulation, NOAA's Climate Prediction Center (CPC) for supplying the global-merged IR data, and NASA for providing the IMERG precipitation data. The authors declare no conflict of interest.

Open Research

The hourly global reanalysis data ERA5 at pressure levels (ECMWF, 2017), CPC-4km half-hourly IR brightness temperature data (Janowiak et al., 2001), NASA GPM IMERG half-hourly precipitation version 6 (Huffman et al., 2019) are used to generate the model data and MCS tracking in this manuscript. The Community Radiative Transfer Model (Johnson et al., 2022) was used to generate the simulated cloud top temperature using WRF-CPM outputs. All the data generated and the code used in this study are open-sourced (Lu, Marsham, et al., 2024).

References

Baidu, M., Schwendike, J., Marsham, J. H., & Bain, C. (2022). Effects of vertical wind shear on intensities of mesoscale convective systems over West and Central Africa. *Atmospheric Science Letters*, *23*(8), e1094. https://doi.org/10.1002/asl.1094

Berg, P., Moseley, C., & Haerter, J. O. (2013). Strong increase in convective precipitation in response to higher temperatures. *Nature Geoscience*, *6*(3), 181–185. https://doi.org/10.1038/ngeo1731

Berthou, S., Rowell, D. P., Kendon, E. J., Roberts, M. J., Stratton, R. A., Crook, J. A., & Wilcox, C. (2019). Improved climatological precipitation characteristics over West Africa at convection-permitting scales. *Climate Dynamics*, *53*(3), 1991–2011. https://doi.org/10.1007/s00382-019-04759-4

Bouniol, D., Roca, R., Fiolleau, T., & Poan, D. E. (2016). Macrophysical, Microphysical, and Radiative Properties of Tropical Mesoscale Convective Systems over Their Life Cycle. *Journal of Climate*, *29*(9), 3353–3371. https://doi.org/10.1175/JCLI-D-15-0551.1

Chen, G., Sha, W., & Iwasaki, T. (2009). Diurnal variation of precipitation over southeastern China: Spatial distribution and its seasonality. *Journal of Geophysical Research: Atmospheres*, *114*(D13). https://doi.org/10.1029/2008JD011103

Chen, H., Yu, R., Li, J., Yuan, W., & Zhou, T. (2010). Why Nocturnal Long-Duration Rainfall Presents an Eastward-Delayed Diurnal Phase of Rainfall down the Yangtze River Valley. *Journal of Climate*, *23*(4), 905–917. https://doi.org/10.1175/2009JCLI3187.1

Chen, X., Leung, L. R., Feng, Z., & Song, F. (2022). Crucial Role of Mesoscale Convective Systems in the Vertical Mass, Water, and Energy Transports of the South Asian Summer Monsoon. *Journal of Climate*, *35*(1), 91–108. https://doi.org/10.1175/JCLI-D-21-0124.1

Chen, X., Leung, L. R., Feng, Z., & Yang, Q. (2022). Precipitation-Moisture Coupling Over Tropical Oceans: Sequential Roles of Shallow, Deep, and Mesoscale Convective Systems. *Geophysical Research Letters*, *49*(7), e2022GL097836. https://doi.org/10.1029/2022GL097836

Cheng, T. F., Dong, Q., Dai, L., & Lu, M. (2022). A Dual Regime of Mesoscale Convective Systems in the East Asian Monsoon Annual Cycle. *Journal of Geophysical Research: Atmospheres*, *127*(13), e2022JD036523. https://doi.org/10.1029/2022JD036523

Cintineo, R., Otkin, J. A., Xue, M., & Kong, F. (2014). Evaluating the Performance of Planetary Boundary Layer and Cloud Microphysical Parameterization Schemes in Convection-Permitting Ensemble Forecasts Using Synthetic GOES-13 Satellite Observations. *Monthly Weather Review*, *142*(1), 163–182. https://doi.org/10.1175/MWR-D-13-00143.1

Clark, A. J., Bullock, R. G., Jensen, T. L., Xue, M., & Kong, F. (2014). Application of Object-Based Time-Domain Diagnostics for Tracking Precipitation Systems in Convection-Allowing Models. *Weather and Forecasting*, *29*(3), 517–542. https://doi.org/10.1175/WAF-D-13-00098.1

Collins, W., Rasch, P., Boville, B., Hack, J., Mccaa, J., Williamson, D., & Kiehl, J. (2004). Description of the NCAR community atmosphere model (CAM 3.0). *NCAR Technical Note*, *TN-464+STR*.

Dong, F., Zhi, X., Zhu, S., Zhang, L., Ge, F., Fan, Y., et al. (2023). Principal Modes of Diurnal Cycle of Rainfall over South China during the Presummer Rainy Season. *Journal of Climate*, *36*(8), 2457–2470. https://doi.org/10.1175/JCLI-D-22-0284.1

ECMWF. (2017). European Centre for Medium-Range Weather Forecasts, ERA5 reanalysis data (updated monthly) [Data set]. Dataset. Retrieved from https://cds.climate.copernicus.eu/cdsapp#!/home

Eyring, V., Bony, S., Meehl, G. A., Senior, C. A., Stevens, B., Stouffer, R. J., & Taylor, K. E. (2016). Overview of the Coupled Model Intercomparison Project Phase 6 (CMIP6) experimental design and organization. *Geoscientific Model Development*, *9*(5), 1937–1958. https://doi.org/10.5194/gmd-9-1937-2016

Feng, Z., Leung, L. R., Liu, N., Wang, J., Houze Jr, R. A., Li, J., et al. (2021). A Global High-Resolution Mesoscale Convective System Database Using Satellite-Derived Cloud Tops, Surface Precipitation, and Tracking. *Journal of Geophysical Research: Atmospheres*, *126*(8), e2020JD034202. https://doi.org/10.1029/2020JD034202

Fitzpatrick, R. G. J., Parker, D. J., Marsham, J. H., Rowell, D. P., Guichard, F. M., Taylor, C. M., et al. (2020). What Drives the Intensification of Mesoscale Convective Systems over the West African Sahel under Climate Change? *Journal of Climate*, *33*(8), 3151–3172. https://doi.org/10.1175/JCLI-D-19-0380.1

Giorgi, F., Jones, C., & Asrar, G. R. (2009). Addressing climate information needs at the regional level: the CORDEX framework. *World Meteorological Organization (WMO) Bulletin*, *58*(3), 175.

Guo, Y., Fu, Q., Leung, L. R., Na, Y., & Lu, R. (2023). Trends in Warm Season Mesoscale Convective Systems Over Asia in 2001–2020. *Journal of Geophysical Research: Atmospheres*, *128*(17), e2023JD038969. https://doi.org/10.1029/2023JD038969

Guo, Z., Fang, J., Sun, X., Yang, Y., & Tang, J. (2019). Sensitivity of Summer Precipitation Simulation to Microphysics Parameterization Over Eastern China: Convection-Permitting Regional Climate Simulation. *Journal of Geophysical Research: Atmospheres*, *124*(16), 9183–9204. https://doi.org/10.1029/2019JD030295

Guo, Z., Fang, J., Sun, X., Tang, J., Yang, Y., & Tang, J. (2020). Decadal long convection-permitting regional climate simulations over eastern China: evaluation of diurnal cycle of precipitation. *Climate Dynamics*, *54*(3–4), 1329–1349. https://doi.org/10.1007/s00382-019-05061-z

Guo, Z., Tang, J., Tang, J., Wang, S., Yang, Y., Luo, W., & Fang, J. (2022). Object-Based Evaluation of Precipitation Systems in Convection-Permitting Regional Climate Simulation Over Eastern China. *Journal of Geophysical Research: Atmospheres*, *127*(1), e2021JD035645. https://doi.org/10.1029/2021JD035645

Haberlie, A. M., Ashley, W. S., Gensini, V. A., & Michaelis, A. C. (2023). The ratio of mesoscale convective system precipitation to total precipitation increases in future climate change scenarios. *Npj Climate and Atmospheric Science*, *6*(1), 1–5. https://doi.org/10.1038/s41612-023-00481-5

Halladay, K., Berthou, S., & Kendon, E. (2024). Improving land surface feedbacks to the atmosphere in convection-permitting climate simulations for Europe. *Climate Dynamics*, *62*(7), 6079–6096. https://doi.org/10.1007/s00382-024-07192-4

Hersbach, H., Bell, B., Berrisford, P., Hirahara, S., Horányi, A., Muñoz-Sabater, J., et al. (2020). The ERA5 global reanalysis. *Quarterly Journal of the Royal Meteorological Society*, *146*(730), 1999–2049. https://doi.org/10.1002/qj.3803

Hong, S.-Y., Dudhia, J., & Chen, S.-H. (2004). A Revised Approach to Ice Microphysical Processes for the Bulk Parameterization of Clouds and Precipitation. *Monthly Weather Review*, *132*(1), 103–120. https://doi.org/10.1175/1520-0493(2004)132<0103:ARATIM>2.0.CO;2

Hong, S.-Y., Noh, Y., & Dudhia, J. (2006). A New Vertical Diffusion Package with an Explicit Treatment of Entrainment Processes. *Monthly Weather Review*, *134*(9), 2318–2341. https://doi.org/10.1175/MWR3199.1

Houze, J. R. A. (2014). *Cloud Dynamics*. Academic Press.

Houze Jr., R. A. (2004). Mesoscale convective systems. *Reviews of Geophysics*, *42*(4). https://doi.org/10.1029/2004RG000150

Houze, R. A. (2018). 100 Years of Research on Mesoscale Convective Systems. *Meteorological Monographs*, *59*(1), 17.1-17.54. https://doi.org/10.1175/AMSMONOGRAPHS-D-18-0001.1

Huffman, G. J., Stocker, E. F., Bolvin, D. T., Nelkin, E. J., & Jackson, T. (2019). GPM IMERG Final Precipitation L3 Half Hourly 0.1 degree x 0.1 degree V06, Greenbelt, MD, Goddard Earth Sciences Data and Information Services Center (GES DISC) [Data set]. Dataset. https://doi.org/10.5067/GPM/IMERG/3B-HH/06

Janowiak, J. E., Joyce, R. J., & Yarosh, Y. (2001). A Real-Time Global Half-Hourly Pixel-Resolution Infrared Dataset and Its Applications. *Bulletin of the American Meteorological Society*, *82*(2), 205–218. https://doi.org/10.1175/1520-0477(2001)082<0205:ARTGHH>2.3.CO;2

Jeworrek, J., West, G., & Stull, R. (2021). WRF Precipitation Performance and Predictability for Systematically Varied Parameterizations over Complex Terrain. *Weather and Forecasting*, *36*(3), 893–913. https://doi.org/10.1175/WAF-D-20-0195.1

Johnson, B., Dang, C., Rosinski, J., YingtaoMa, Kasprzyk, P., & StegmannJCSDA. (2022, August 19). JCSDA/crtm: v2.3.0 for EMC tag (Version v2.3.0_emc). Zenodo. https://doi.org/10.5281/zenodo.7011073

Karki, R., ul Hasson, S., Gerlitz, L., Schickhoff, U., Scholten, T., & Böhner, J. (2017). Quantifying the added value of convection-permitting climate simulations in complex terrain: a systematic evaluation of WRF over the Himalayas. *Earth System Dynamics*, *8*(3), 507–528. https://doi.org/10.5194/esd-8-507-2017

Kendon, E. J., Stratton, R. A., Tucker, S., Marsham, J. H., Berthou, S., Rowell, D. P., & Senior, C. A. (2019). Enhanced future changes in wet and dry extremes over Africa at convection-permitting scale. *Nature Communications*, *10*(1), 1794. https://doi.org/10.1038/s41467-019-09776-9

Kidd, C., Becker, A., Huffman, G. J., Muller, C. L., Joe, P., Skofronick-Jackson, G., & Kirschbaum, D. B. (2017). So, How Much of the Earth's Surface Is Covered by Rain Gauges? *Bulletin of the American Meteorological Society*, *98*(1), 69–78. https://doi.org/10.1175/BAMS-D-14-00283.1

Klein, C., Jackson, L. S., Parker, D. J., Marsham, J. H., Taylor, C. M., Rowell, D. P., et al. (2021). Combining CMIP data with a regional convection-permitting model and observations to project extreme rainfall under climate change. *Environmental Research Letters*, *16*(10), 104023. https://doi.org/10.1088/1748-9326/ac26f1

Klein, C., Nkrumah, F., Taylor, C. M., & Adefisan, E. A. (2021). Seasonality and Trends of Drivers of Mesoscale Convective Systems in Southern West Africa. *Journal of Climate*, *34*(1), 71–87. https://doi.org/10.1175/JCLI-D-20-0194.1

Kukulies, J., Chen, D., & Curio, J. (2021). The Role of Mesoscale Convective Systems in Precipitation in the Tibetan Plateau Region. *Journal of Geophysical Research: Atmospheres*, *126*(23), e2021JD035279. https://doi.org/10.1029/2021JD035279

Kukulies, J., Lai, H.-W., Curio, J., Feng, Z., Lin, C., Li, P., et al. (2023). Mesoscale convective systems in the third pole region: Characteristics, mechanisms and impact on precipitation. *Frontiers in Earth Science*, *11*. Retrieved from https://www.frontiersin.org/articles/10.3389/feart.2023.1143380

Kundu, P. K. (1976). Ekman Veering Observed near the Ocean Bottom. *Journal of Physical Oceanography*, *6*(2), 238–242. https://doi.org/10.1175/1520-0485(1976)006<0238:EVONTO>2.0.CO;2

Li, J., Chen, H., Jiang, X., & Li, P. (2024). Diurnal variations of summer rainfall response to large-scale circulations and low-level winds over the Sichuan Basin. *Climate Dynamics*, *62*(3), 2041–2056. https://doi.org/10.1007/s00382-023-07009-w

Li, N., Guo, J., Wu, M., Zhang, F., Guo, X., Sun, Y., et al. (2024). Low-Level Jet and Its Effect on the Onset of Summertime Nocturnal Rainfall in Beijing. *Geophysical Research Letters*, *51*(20), e2024GL110840. https://doi.org/10.1029/2024GL110840

Li, P., Moseley, C., Prein, A. F., Chen, H., Li, J., Furtado, K., & Zhou, T. (2020). Mesoscale Convective System Precipitation Characteristics over East Asia. Part I: Regional Differences and Seasonal Variations. *Journal of Climate*, *33*(21), 9271–9286. https://doi.org/10.1175/JCLI-D-20-0072.1

Li, P., Furtado, K., Zhou, T., Chen, H., Li, J., Guo, Z., & Xiao, C. (2020). The diurnal cycle of East Asian summer monsoon precipitation simulated by the Met Office Unified Model at convection-permitting scales. *Climate Dynamics*, *55*(1), 131–151. https://doi.org/10.1007/s00382-018-4368-z

Li, P., Furtado, K., Zhou, T., Chen, H., & Li, J. (2021). Convection-permitting modelling improves simulated precipitation over the central and eastern Tibetan Plateau. *Quarterly Journal of the Royal Meteorological Society*, *147*(734), 341–362. https://doi.org/10.1002/qj.3921

Li, P., Song, F., Chen, H., Li, J., Prein, A. F., Zhang, W., et al. (2023). Intensification of Mesoscale Convective Systems in the East Asian Rainband Over the Past Two Decades. *Geophysical Research Letters*, *50*(16), e2023GL103595. https://doi.org/10.1029/2023GL103595

Li, P., Muetzelfeldt, M., Schiemann, R., Chen, H., Li, J., Furtado, K., & Zhuang, M. (2023). Sensitivity of simulated mesoscale convective systems over East Asia to the treatment of convection in a high-resolution GCM. *Climate Dynamics*, *60*(9), 2783–2801. https://doi.org/10.1007/s00382-022-06471-2

Lipzig, N. P. M. van, Walle, J. V. de, Belušić, D., Berthou, S., Coppola, E., Demuzere, M., et al. (2023). Representation of precipitation and top-of-atmosphere radiation in a multi-model convection-permitting ensemble for the Lake Victoria Basin (East-Africa). *Climate Dynamics*, *60*(11), 4033–4054. https://doi.org/10.1007/s00382-022-06541-5

Liu, J., Yang, L., Jiang, J., Yuan, W., & Duan, Z. (2021). Mapping diurnal cycles of precipitation over China through clustering. *Journal of Hydrology*, *592*, 125804. https://doi.org/10.1016/j.jhydrol.2020.125804

Liu, Z., Gao, Y., & Zhang, G. (2022). How well can a convection-permitting-modelling improve the simulation of summer precipitation diurnal cycle over the Tibetan Plateau? *Climate Dynamics*, *58*(11), 3121–3138. https://doi.org/10.1007/s00382-021-06090-3

Long, L., He, L., Li, J., Zhang, W., & Zhang, Y. (2023). Climatic characteristics of mesoscale convective systems in the warm season in North China. *Meteorology and Atmospheric Physics*, *135*(2), 21. https://doi.org/10.1007/s00703-023-00958-1

Lu, Y., Tang, J., Xu, X., Tang, Y., & Fang, J. (2024). Characteristics of Warm-Season Mesoscale Convective Systems Over the Yangtze–Huaihe River Basin (YHR): Comparison Between Radar and Satellite. *Journal of Geophysical Research: Atmospheres*, *129*(1), e2023JD038924. https://doi.org/10.1029/2023JD038924

Lu, Y., Marsham, J. H., Tang, J., Parker, D. J., & Fang, J. (2024). Summer mesoscale convective systems in convection-permitting simulation using WRF over East China [Data set]. Dataset, Zenodo. https://doi.org/10.5281/zenodo.11223708

Lucas-Picher, P., Argüeso, D., Brisson, E., Tramblay, Y., Berg, P., Lemonsu, A., et al. (2021). Convection-permitting modeling with regional climate models: Latest developments and next steps. *WIREs Climate Change*, *12*(6), e731. https://doi.org/10.1002/wcc.731

Ma, M., Hui, P., Liu, D., Zhou, P., & Tang, J. (2022). Convection-permitting regional climate simulations over Tibetan Plateau: re-initialization versus spectral nudging. *Climate Dynamics*, *58*(5), 1719–1735. https://doi.org/10.1007/s00382-021-05988-2

Ma, Y.-F., Wang, Y., Xian, T., Tian, G., Lu, C., Mao, X., & Wang, L.-P. (2024). Impact of PBL schemes on multiscale WRF modeling over complex terrain, Part I: Mesoscale simulations. *Atmospheric Research*, *297*, 107117. https://doi.org/10.1016/j.atmosres.2023.107117

Maybee, B., Marsham, J. H., Klein, C. M., Parker, D. J., Barton, E. J., Taylor, C. M., et al. (2024). Wind Shear Effects in Convection–Permitting Models Influence MCS Rainfall and Forcing of Tropical Circulation. *Geophysical Research Letters*, *51*(17), e2024GL110119. https://doi.org/10.1029/2024GL110119

Meredith, E. P., Ulbrich, U., Rust, H. W., & Truhetz, H. (2021). Present and future diurnal hourly precipitation in 0.11° EURO-CORDEX models and at convection-permitting resolution. *Environmental Research Communications*, *3*(5), 055002. https://doi.org/10.1088/2515-7620/abf15e

Mulholland, J. P., Peters, J. M., & Morrison, H. (2021). How Does LCL Height Influence Deep Convective Updraft Width? *Geophysical Research Letters*, *48*(13), e2021GL093316. https://doi.org/10.1029/2021GL093316

Niu, G.-Y., Yang, Z.-L., Mitchell, K. E., Chen, F., Ek, M. B., Barlage, M., et al. (2011). The community Noah land surface model with multiparameterization options (Noah-MP): 1. Model description and evaluation with local-scale measurements. *Journal of Geophysical Research: Atmospheres*, *116*(D12). https://doi.org/10.1029/2010JD015139

Ou, T., Chen, D., Chen, X., Lin, C., Yang, K., Lai, H.-W., & Zhang, F. (2020). Simulation of summer precipitation diurnal cycles over the Tibetan Plateau at the gray-zone grid spacing for cumulus parameterization. *Climate Dynamics*, *54*(7), 3525–3539. https://doi.org/10.1007/s00382-020-05181-x

Prein, A. F., Gobiet, A., Suklitsch, M., Truhetz, H., Awan, N. K., Keuler, K., & Georgievski, G. (2013). Added value of convection permitting seasonal simulations. *Climate Dynamics*, *41*(9), 2655–2677. https://doi.org/10.1007/s00382-013-1744-6

Prein, Andreas F., Langhans, W., Fosser, G., Ferrone, A., Ban, N., Goergen, K., et al. (2015). A review on regional convection-permitting climate modeling: Demonstrations, prospects, and challenges. *Reviews of Geophysics*, *53*(2), 323–361. https://doi.org/10.1002/2014RG000475

Prein, Andreas F., Liu, C., Ikeda, K., Trier, S. B., Rasmussen, R. M., Holland, G. J., & Clark, M. P. (2017). Increased rainfall volume from future convective storms in the US. *Nature Climate Change*, *7*(12), 880–884. https://doi.org/10.1038/s41558-017-0007-7

Prein, Andreas F., Liu, C., Ikeda, K., Bullock, R., Rasmussen, R. M., Holland, G. J., & Clark, M. (2020). Simulating North American mesoscale convective systems with a convection-permitting climate model. *Climate Dynamics*, *55*(1), 95–110. https://doi.org/10.1007/s00382-017-3993-2

Rasmussen, K. L., Prein, A. F., Rasmussen, R. M., Ikeda, K., & Liu, C. (2020). Changes in the convective population and thermodynamic environments in convection-permitting regional climate simulations over the United States. *Climate Dynamics*, *55*(1), 383–408. https://doi.org/10.1007/s00382-017-4000-7

Richardson, Y. P. (1999). *The influence of horizontal variations in vertical shear and low-level moisture on numerically simulated convective storms - ProQuest*. The University of Oklahoma. Retrieved from https://www.proquest.com/openview/05d1960d731851e69b538b4458a08503/1?pq-origsite=gscholar&cbl=18750&diss=y

Scaff, L., Prein, A. F., Li, Y., Liu, C., Rasmussen, R., & Ikeda, K. (2020). Simulating the convective precipitation diurnal cycle in North America's current and future climate. *Climate Dynamics*, *55*(1), 369–382. https://doi.org/10.1007/s00382-019-04754-9

Schumacher, R. S., & Rasmussen, K. L. (2020). The formation, character and changing nature of mesoscale convective systems. *Nature Reviews Earth & Environment*, *1*(6), 300–314. https://doi.org/10.1038/s43017-020-0057-7

Senior, C. A., Marsham, J. H., Berthou, S., Burgin, L. E., Folwell, S. S., Kendon, E. J., et al. (2021). Convection-Permitting Regional Climate Change Simulations for Understanding Future Climate and Informing Decision-Making in Africa. *Bulletin of the American Meteorological Society*, *102*(6), E1206–E1223. https://doi.org/10.1175/BAMS-D-20-0020.1

Skamarock, W. C., Klemp, J. B., Dudhia, J., Gill, D. O., Barker, D. M., Duda, M. G., et al. (2019). A Description of the Advanced Research WRF Version 4. *NCAR Tech. Note Ncar/Tn-556+ Str*, *145*.

Stevens, B., Adami, S., Ali, T., Anzt, H., Aslan, Z., Attinger, S., et al. (2024). Earth Virtualization Engines (EVE). *Earth System Science Data*, *16*(4), 2113–2122. https://doi.org/10.5194/essd-16-2113-2024

Tan, J., Huffman, G. J., Bolvin, D. T., & Nelkin, E. J. (2019). IMERG V06: Changes to the Morphing Algorithm. *Journal of Atmospheric and Oceanic Technology*, *36*(12), 2471–2482. https://doi.org/10.1175/JTECH-D-19-0114.1

Tang, J., Lu, Y., Wang, S., Guo, Z., Lu, Y., & Fang, J. (2023). Projection of Hourly Extreme Precipitation Using the WRF Model Over Eastern China. *Journal of Geophysical Research: Atmospheres*, *128*(1), e2022JD036448. https://doi.org/10.1029/2022JD036448

Teramura, H., Sato, T., & Tamura, K. (2019). Observed Evidence of Enhanced Probability of Mesoscale Convective System Initiations due to Land Surface Heterogeneity in Semiarid East Asia. *SOLA*, *15*(0), 143–148. https://doi.org/10.2151/sola.2019-026

Wang, C., Chen, X., Zhao, K., & Peng, C.-H. (2024). Synoptic Control on the Initiation and Rainfall Characteristics of Warm-Season MCSs Over the South China Coast. *Journal of Geophysical Research: Atmospheres*, *129*(8), e2023JD039232. https://doi.org/10.1029/2023JD039232

Wang, D., Giangrande, S. E., Schiro, K. A., Jensen, M. P., & Houze Jr., R. A. (2019). The Characteristics of Tropical and Midlatitude Mesoscale Convective Systems as Revealed by Radar Wind Profilers. *Journal of Geophysical Research: Atmospheres*, *124*(8), 4601–4619. https://doi.org/10.1029/2018JD030087

Weisman, M. L., & Rotunno, R. (2004). “A Theory for Strong Long-Lived Squall Lines” Revisited. *Journal of the Atmospheric Sciences*, *61*(4), 361–382. https://doi.org/10.1175/1520-0469(2004)061<0361:ATFSLS>2.0.CO;2

Weng, F., Han, Y., van Delst, P., Liu, Q., Kleespies, T., Yan, B., & Marshall, J. L. (2005). JCSDA Community Radiative Transfer Model (CRTM).

Wu, A., & Li, G. (2023). Roles of the Topographically-Affected Boundary Layer Low-Level Jet in the Moisture Transport Process of Nocturnal Rainstorms in Mountainous Areas around the Western Sichuan Basin. *Atmosphere*, *14*(1), 84. https://doi.org/10.3390/atmos14010084

Wu, M., & Luo, Y. (2016). Mesoscale observational analysis of lifting mechanism of a warm-sector convective system producing the maximal daily precipitation in China mainland during pre-summer rainy season of 2015. *Journal of Meteorological Research*, *30*(5), 719–736. https://doi.org/10.1007/s13351-016-6089-8

Yang, Q., Houze, R. A., Leung, L. R., & Feng, Z. (2017). Environments of Long-Lived Mesoscale Convective Systems Over the Central United States in Convection Permitting Climate Simulations. *Journal of Geophysical Research: Atmospheres*, *122*(24), 13,288-13,307. https://doi.org/10.1002/2017JD027033

Yang, X., Fei, J., Huang, X., Cheng, X., Carvalho, L. M. V., & He, H. (2015). Characteristics of Mesoscale Convective Systems over China and Its Vicinity Using Geostationary Satellite FY2. *Journal of Climate*, *28*(12), 4890–4907. https://doi.org/10.1175/JCLI-D-14-00491.1

Ye, H., Fetzer, E. J., Wong, S., & Lambrigtsen, B. H. (2017). Rapid decadal convective precipitation increase over Eurasia during the last three decades of the 20th century. *Science Advances*, *3*(1), e1600944. https://doi.org/10.1126/sciadv.1600944

Yun, Y., Liu, C., Luo, Y., Liang, X., Huang, L., Chen, F., & Rasmmusen, R. (2020). Convection-permitting regional climate simulation of warm-season precipitation over Eastern China. *Climate Dynamics*, *54*(3), 1469–1489. https://doi.org/10.1007/s00382-019-05070-y

Yun, Y., Liu, C., Luo, Y., & Gao, W. (2021). Warm-season mesoscale convective systems over eastern China: convection-permitting climate model simulation and observation. *Climate Dynamics*, *57*(11), 3599–3617. https://doi.org/10.1007/s00382-021-05994-4

Zhang, Y., Chen, H., Li, P., & Li, J. (2025). The characteristics of summer mesoscale convective systems with different moving paths over Southwest China. *Climate Dynamics*, *63*(1), 77. https://doi.org/10.1007/s00382-025-07586-y

Zhao, M. (2022). A Study of AR-, TS-, and MCS-Associated Precipitation and Extreme Precipitation in Present and Warmer Climates. *Journal of Climate*, *35*(2), 479–497. https://doi.org/10.1175/JCLI-D-21-0145.1

Zhao, Y., Liu, C., Wang, Y., & Moncrieff, M. W. (2020). Quasi-stationary extreme rain produced by mesoscale convective system on the Mei-Yu front. *Meteorology and Atmospheric Physics*, *132*(5), 721–742. https://doi.org/10.1007/s00703-019-00717-1

Table 1. Physical scheme selected in CP-resolution WRF model

S. no	Physics Scheme	WRF Options	References
1	Cumulus scheme	/	
2	Microphysics scheme	WRF Single-moment Schemes (WSM5)	(Hong et al., 2004)
3	Planetary boundary physics scheme	Yonsei University Scheme (YSU)	(Hong et al., 2006)
4	Shortwave and longwave scheme	CAM shortwave and longwave schemes	(Collins et al., 2004)
5	Land surface	Noah-MP land surface model	(Niu et al., 2011)

Table 2 Complex correlation coefficient and phase angle between 850hPa, 500hPa, 200hPa, wind 500–850hPa wind shear and MCS propagation from WRF and Satellite/ERA5.

		850hPa	500hPa	200hPa	wind shear
WRF	CORR	0.54	0.8	0.85	0.78
	Angle	-78.47	22	6.48	7.02
Sate&ERA5	CORR	0.51	0.62	0.76	0.72
	Angle	-49.56	34.3	-1.05	4.08

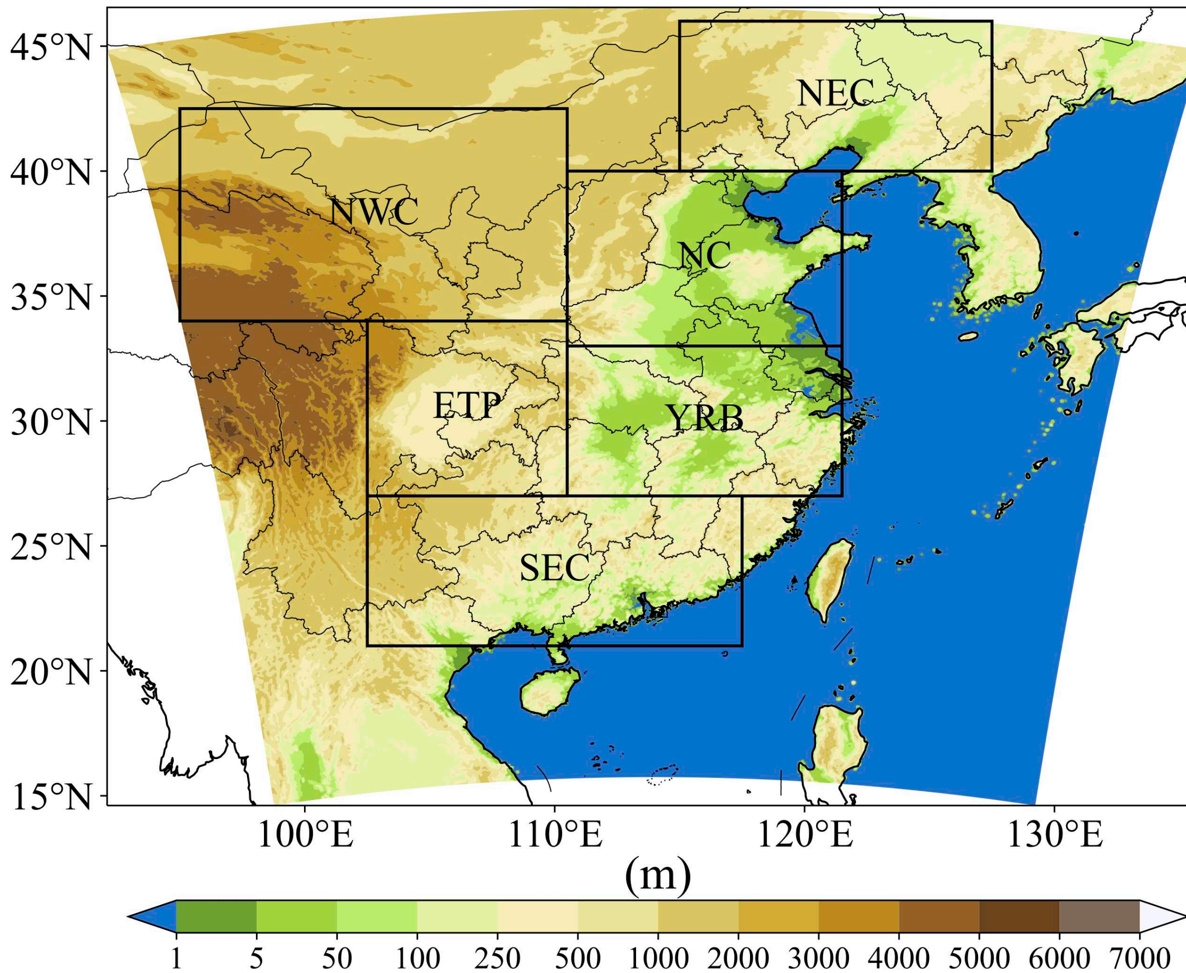

Figure 1. The topography (m) of WRF simulation domain and the 6 sub-regions, namely Southeast China (SEC), Yangtze-Huaihe River Basin (YRB), East Tibetan Plateau (ETP), North China (NC), Northwest China (NWC), and Northeast China (NEC).

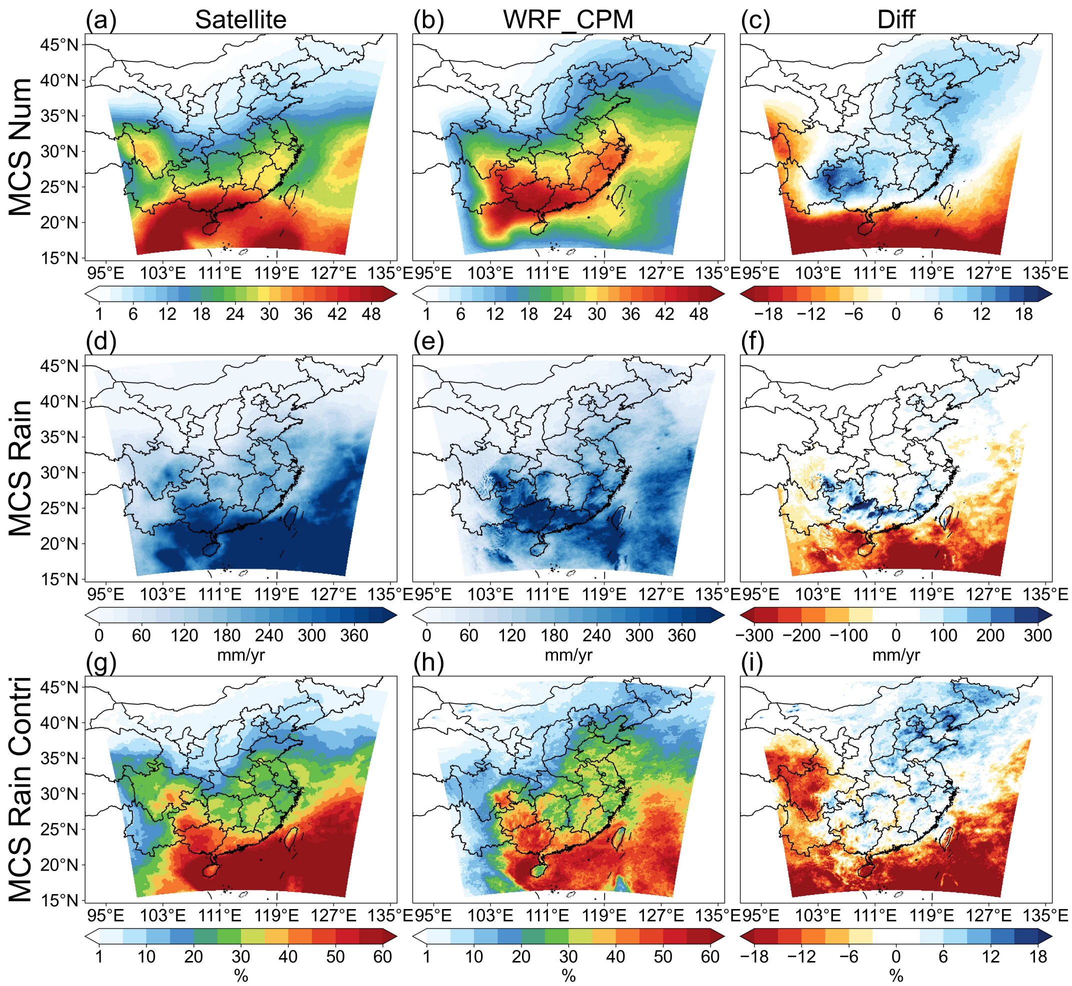

Figure 2. (a, b) The spatial distribution of 22-year average JJA (2000–2021) MCS counts derived from (a) CPC-4km and (b) WRF-CPM, (d, e) the 22-year annual total JJA MCS precipitation (mm) pattern from (d) IMERG and (e) WRF-CPM, (g, h) the spatial distribution of 22-year average MCS rainfall contribution to the total precipitation (%) from (g) IMERG and (h) WRF-CPM, and (c, f, i) the differences of (c) MCS numbers, (f) MCS mean rain rate, and (i) MCS rainfall contribution between CPC-4km/IMERG and WRF-CPM.

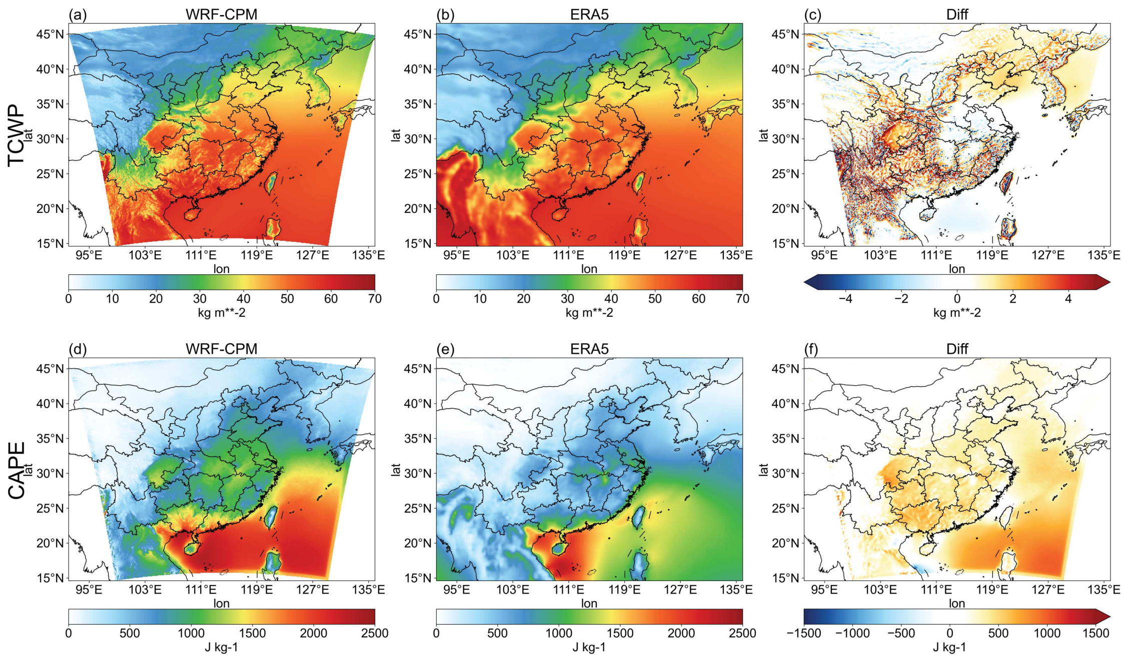

Figure 3. Spatial distribution of 22-year average (a–c) total column water vapor and (d–f) CAPE from (a, d) WRF-CPM, (b, e) ERA5, and (c, f) differences between them

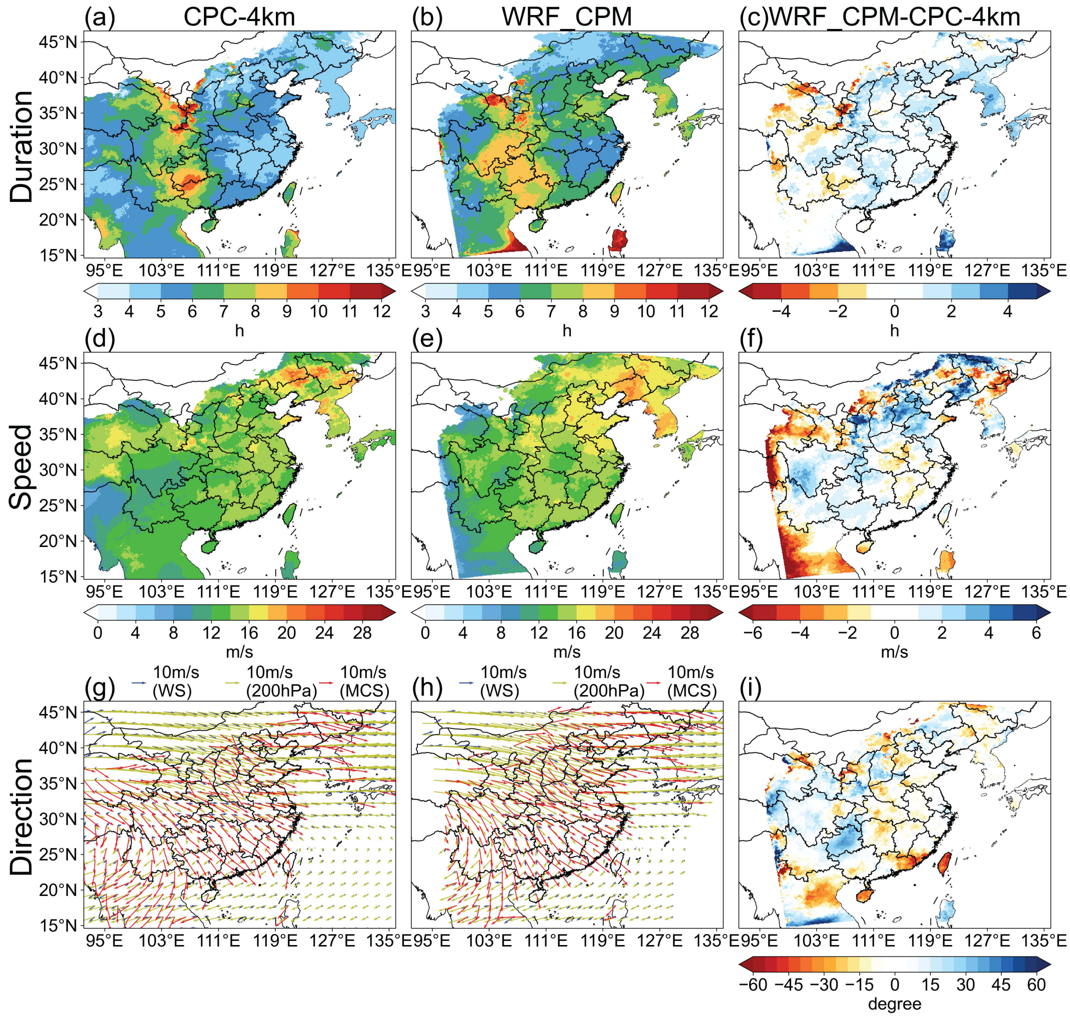

Figure 4. Spatial patterns for median values of MCS features: (a–c) duration, (d–f) propagation speed, and (g–h) MCS propagation vectors (red vectors). Panels show results from (a, d, g) CPC-4km, (b, e, h) WRF-CPM, and (c, f) their differences. (i) Differences of MCS propagation direction. Panels (g–h) also include 22-year JJA average 200hPa (yellow vectors) and 500–850hPa wind shear (blue vectors) from (g) ERA5 and (h) WRF-CPM.

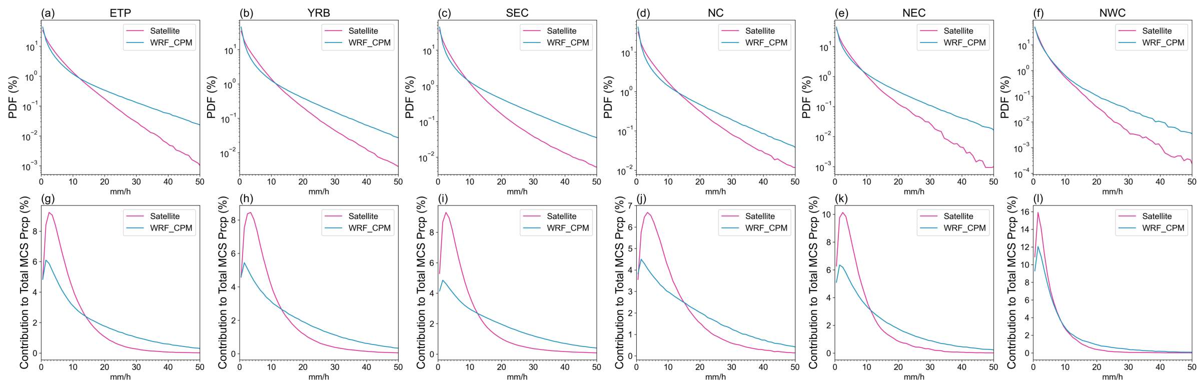

Figure 5. (a–f) The probability density function (PDFs) for MCS precipitation on each pixel during 2000–2021 from IMERG (pink lines) and WRF-CPM (blue lines) over 6 sub-regions. (g–l) The percentage contribution of rainfall amount in each bin to the total precipitation from all bins. The bin size used to construct the plots is 1 mm.

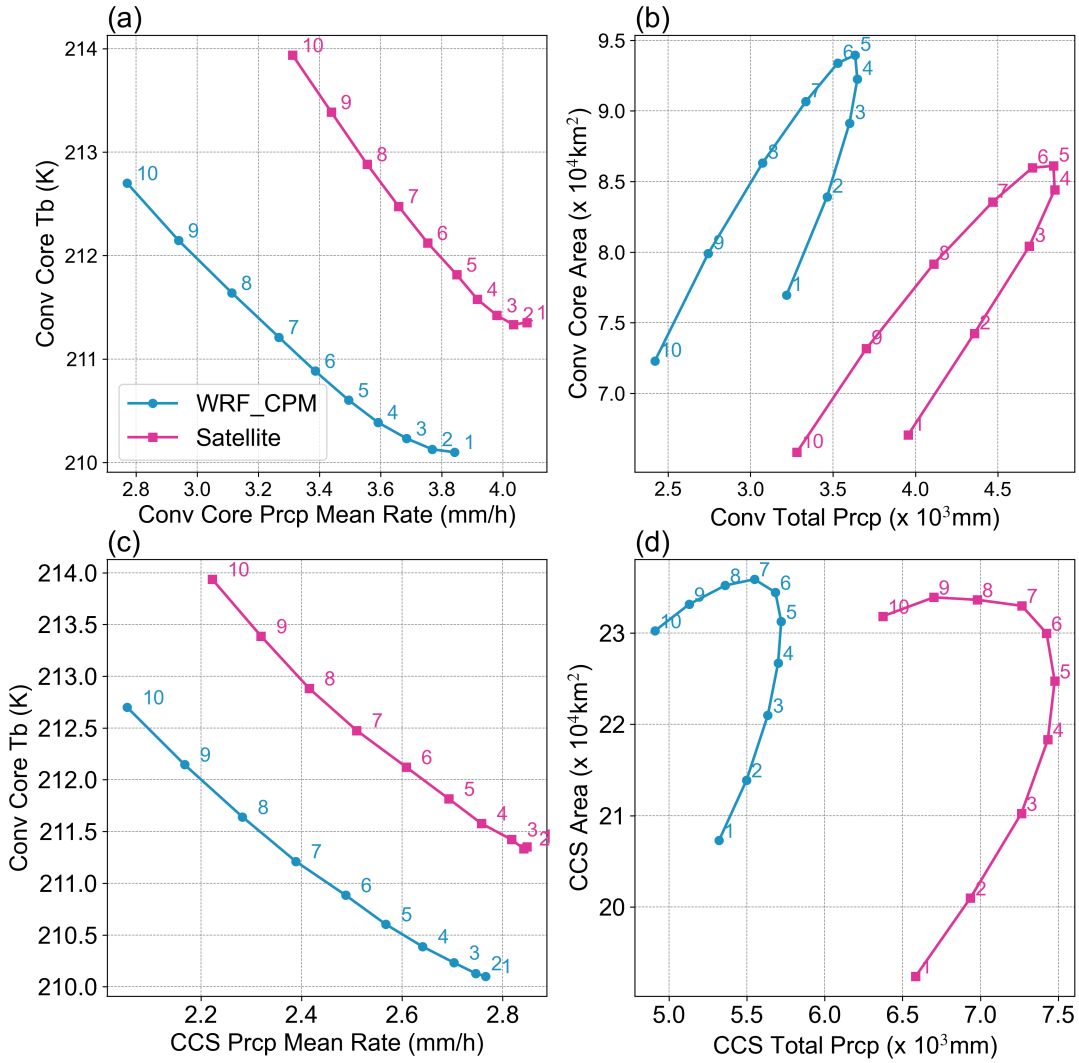

Figure 6. Relationship between average (a) convection core cloud top temperature and average rain rate, (b) convection core area and total precipitation, (c) convection core cloud top temperature and CCS average rain rate, and (d) CCS area and total precipitation within the normalized life cycle of MCSs. The lifetime of each individual MCS is divided into 10 normalized life stages. Stage 1 represents initiation and stage 10 represents dissipation. The property value at each normalized life stage is linearly interpolated from the original life cycle.

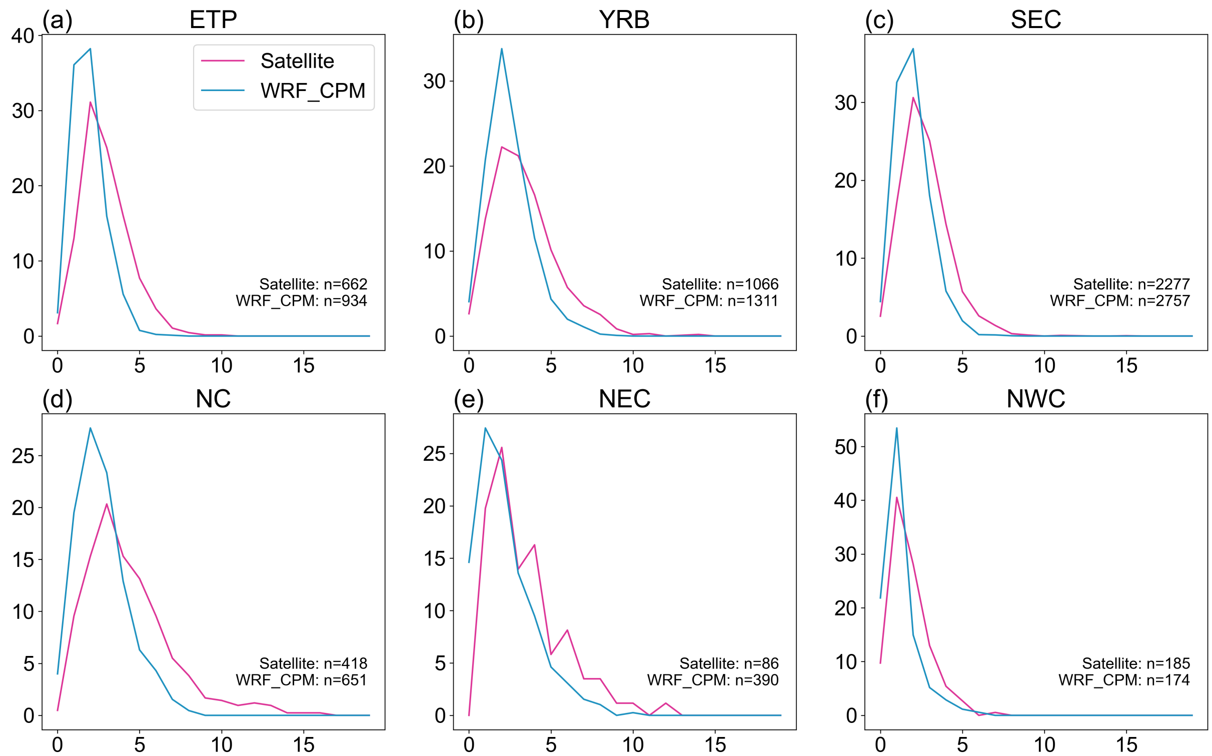

Figure 7. The probability density functions (PDFs) for hourly areal average precipitation (unit: mm/h) of each MCS from CPC-4km (pink lines) and WRF-CPM (blue lines) in 6 sub-regions from 2000–2021. Unit for Y axis is %. The sample counts of MCSs from CPC-4km and WRF-CPM for each sub-region are indicated in the lower right corner of each panel.

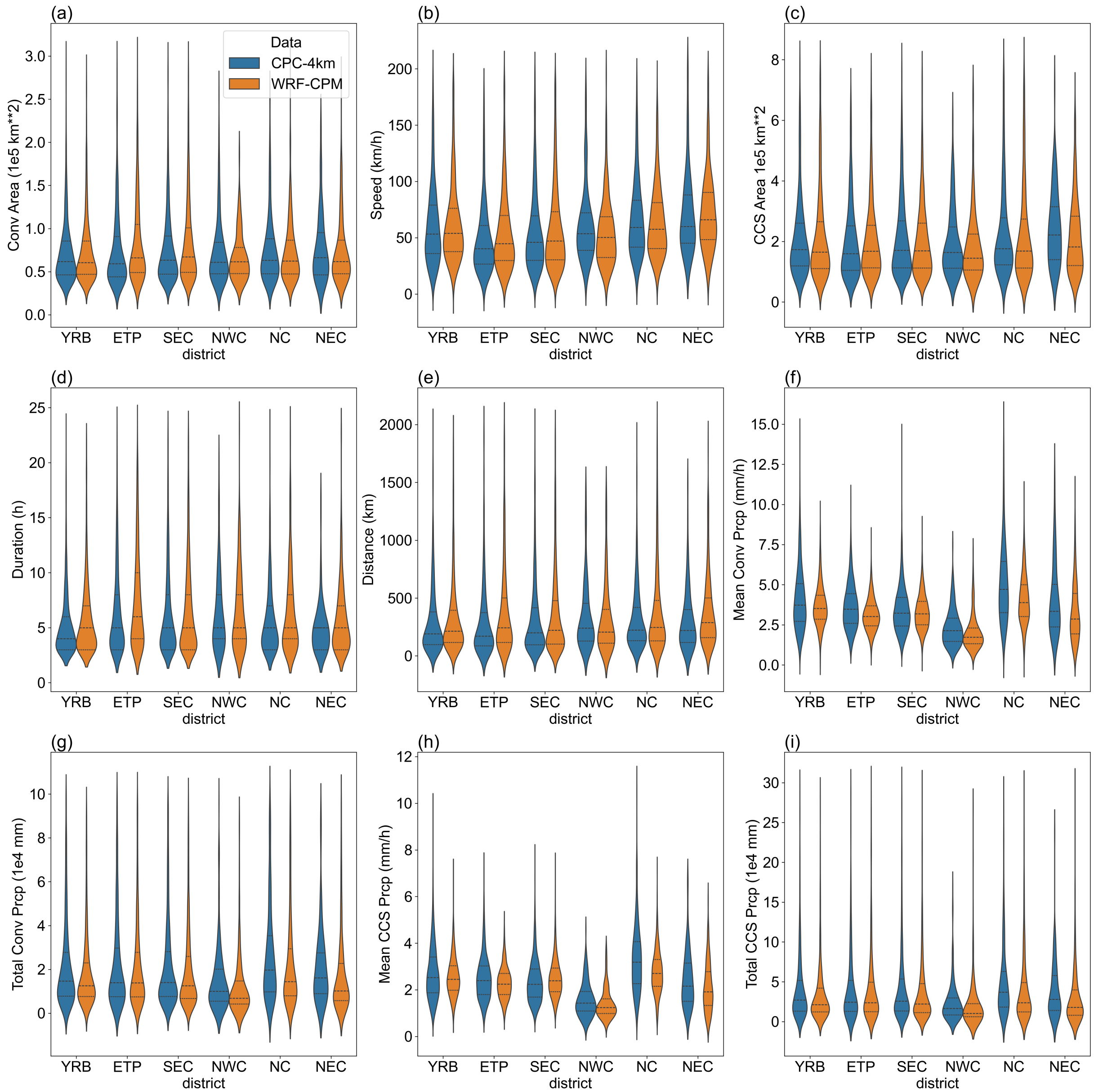

Figure 8. Violin plots for the average (a) convection core area (10^5 km^2), (b) propagation speed (km/h), (c) CCS area (10^5 km^2), (d) duration (h), (e) propagation distance (km), (f) mean convective precipitation (mm/h), (g) total convective precipitation (10^4 mm), (h) CCS precipitation (mm/h), and (i) total CCS precipitation (10^4 mm).

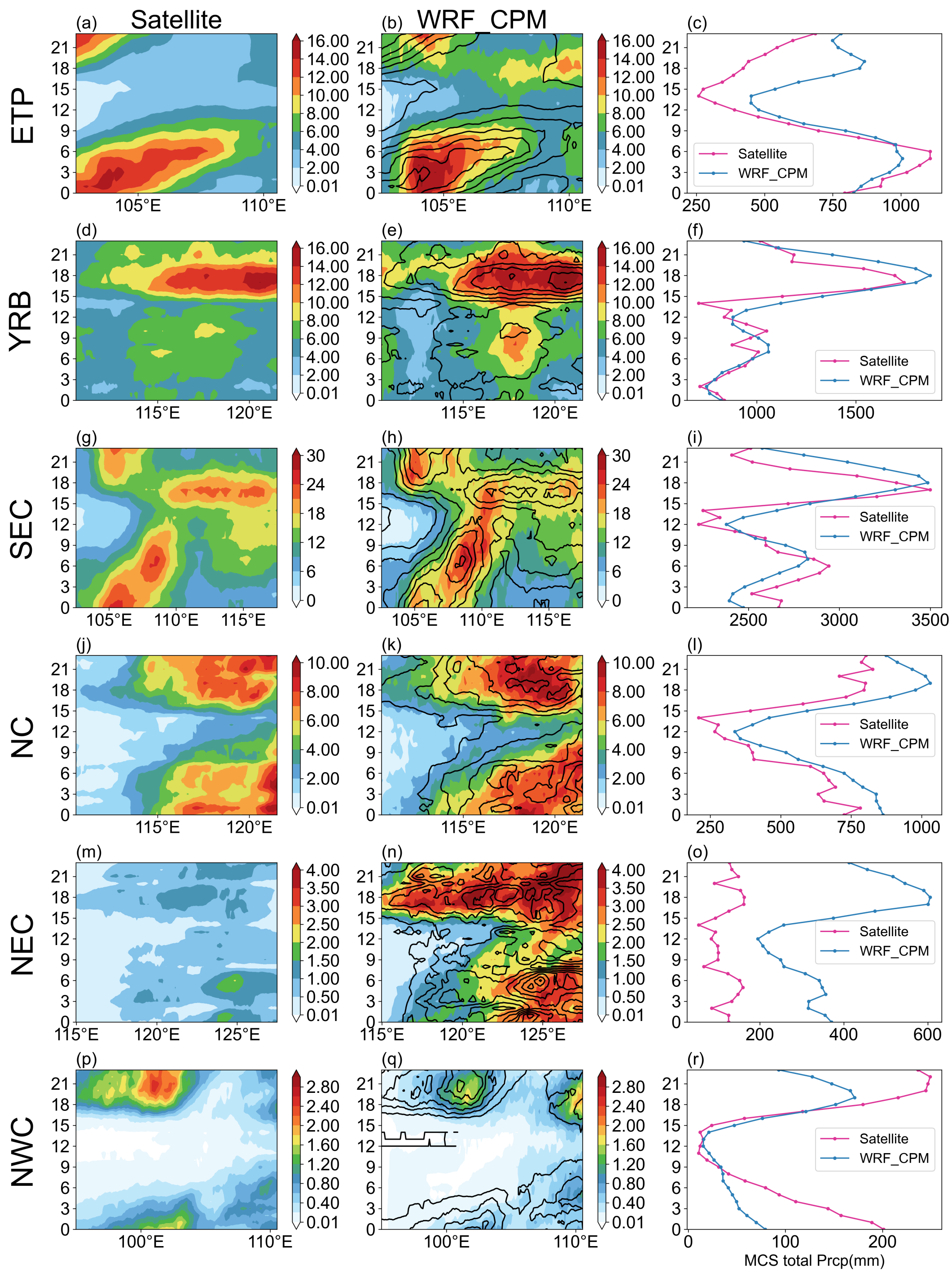

Figure 9. Hovemöller diagram for 22-year annual average JJA MCS precipitation in six sub-regions for (a, e, i, m, q, u) satellite, and (b, f, j, n, r, v) WRF-CPM. (c, g, k ,o ,s, w). The satellite precipitation is overlapped over WRF-CPM precipitation (black contour) in second columns. Diurnal cycle of total JJA MCS precipitation amount in MCS from Satellite (pink line) and WRF-CPM (blue line).

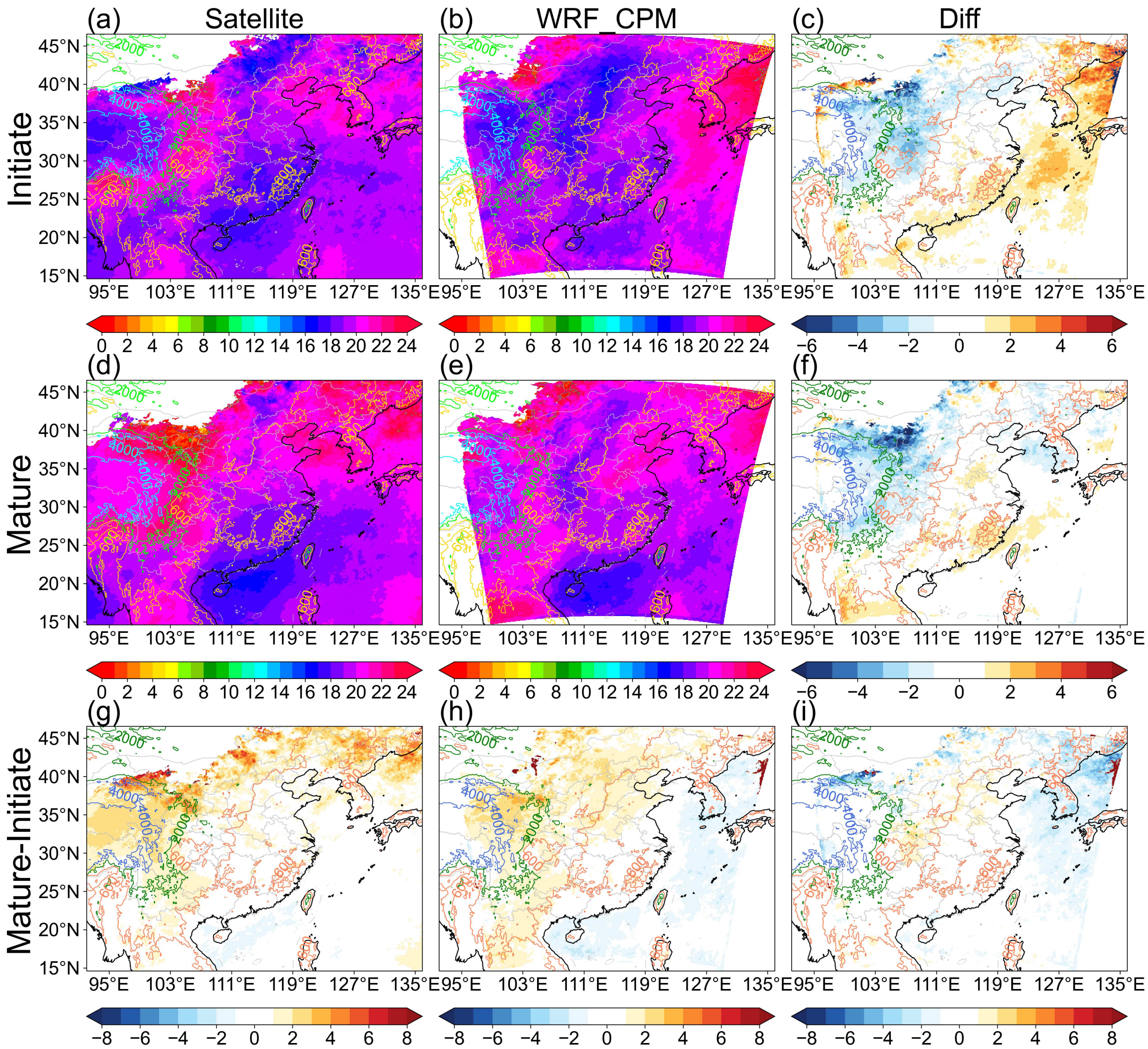

Figure 10. Spatial distribution of 22-year (2000–2021) average diurnal peak hour of MCS (a–c) initiation, (d–f) maturation, and (g–i) hours between mature and initiation from (a, d, g) CPC-4km and (b, e, h) WRF-CPM, and (c, f, i) their differences. The shading is the hour of the day (LST), and the contour is the topography for 4000m, 2000m, and 600m. The gray lines are the boundaries of China and each province, and the black lines represent the coastline.

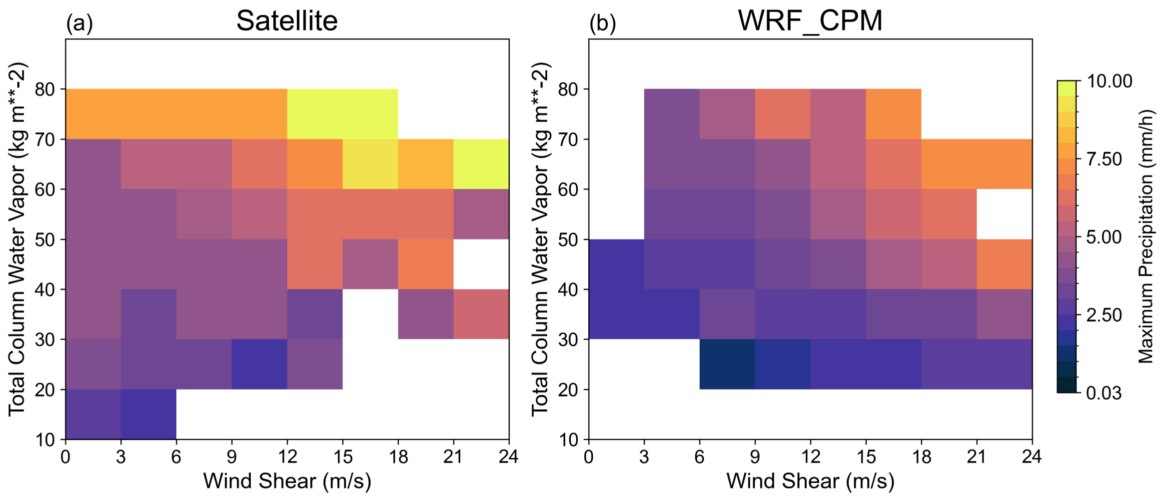

Figure 11 Heatmap of maximum hourly precipitation of each MCS as a function of total column water vapor (TCWV) and 600–925 hPa wind shear from (a) Satellite and (b) WRF-CPM.